

A Wintertime Gulf Coast Squall Line Observed by EDOP Airborne Doppler Radar

G. M. HEYMSFIELD

NASA/Goddard Space Flight Center, Greenbelt, Maryland

J. B. HALVERSON AND I. J. CAYLOR

Joint Center for Earth Systems Technology, University of Maryland Baltimore County, Baltimore, Maryland

(Manuscript received 9 December 1997, in final form 2 December 1998)

ABSTRACT

An extensive wintertime squall line on 13 January 1995 occurring along the U.S. Gulf of Mexico coastline is examined using airborne radar observations combined with conventional data analysis. Flight tracks with the ER-2 Doppler radar (EDOP) mounted on the high-altitude (20 km) ER-2 aircraft provided a unique view of the vertical structure of this line. In this paper, the authors document the squall line structure, and compare and contrast this structure with other published cases.

The squall line had several prominent features that differ from previous studies: 1) the stratiform region was wide in comparison to more typical systems that are 50–100 km wide; 2) the trailing stratiform region consisted of two to three separate embedded trailing bands rather than one continuous band; 3) vertical motions in the trailing stratiform region were nearly twice as strong as previously reported values, with mean values approaching 1 m s^{-1} between 7- and 9-km altitude, and larger values (1.5 m s^{-1}) in the embedded bands; 4) reflectivities were large with mean stratiform values of about 38 dBZ, and maximum convective values of about 55 dBZ; 5) the squall line rear inflow descended to the surface well behind the leading edge ($\sim 200 \text{ km}$); 6) the convective and squall line inflow region exhibited unique microphysics with small graupel or hail falling out of the tilted squall line updraft, and a wavy, elevated melting region associated with the inflow; and 7) the squall-scale transverse circulation was directly coupled with a jet streak thermally direct circulation, and the ascending branch of this direct circulation may have enhanced production of widespread stratiform rainfall. A conceptual model is presented highlighting the features of this squall line and the coupling of the squall line to the larger-scale flow.

1. Introduction

Squall lines have been defined in the literature as mature frontal and nonfrontal lines of convection (e.g., Houze and Hobbs 1982). Precipitation in midlatitude squall lines has been observed to undergo several modes of organization (Bluestein and Jain 1985; Houze et al. 1990). One common type of squall line reported in the literature in tropical and midlatitude environments is the leading convective–trailing stratiform type in which rapidly moving squall lines are often observed with a trailing stratiform rain region typically less than 100 km wide (Houze and Hobbs 1982; Smull and Houze 1987a; Biggerstaff and Houze 1993). This type of squall line has several prominent features: an intermediate region of lower reflectivity called the “transition region” with a predominance of downdrafts (Biggerstaff and Houze 1993), and a rear inflow that allows for intrusion of

midlevel air into the rear boundary of the stratiform region.

Modeling and theoretical studies have demonstrated that the environmental wind shear has an important role in the development and three-dimensional structure of squall lines, particularly the dynamics that govern the vertical updraft and downdraft circulations and the rear-inflow jets that bring dry midlevel air into the rear of the lines (e.g., Rotunno et al. 1988; Weisman et al. 1988; Weisman 1992). These modeling studies have considered the effect of the orientation of line-normal vertical wind shear on squall line structure and evolution. Squall lines forming in environments with weak line-normal shear evolved into upshear-tilted convective lines with a wide band of weaker cells extending behind the leading edge. For environments with strong, deep shears oriented oblique to the line, the squall lines tended to be composed of multiple supercells that are isolated and have three-dimensional structure. Strong line-normal shear squall lines were associated with leading convective–trailing stratiform structure and squall lines with strong alongline shear were asymmetric with a weaker

Corresponding author address: Gerald M. Heymsfield, NASA/GSFC, Code 912, Greenbelt, MD 20771.
E-mail: gerald.heymsfield@gssc.nasa.gov

trailing stratiform component and more severe convection.

Rear-inflow jets commonly occur with squall lines as shown by the 18 cases in Smull and Houze (1987b). They have been characterized in part by whether and where the rear inflow, consisting of drier midlevel air, reaches the surface behind the leading convective edge. Weisman performed a two-dimensional cloud-resolving model study that suggests the morphology of the rear inflow is related to 1) storm internal generating mechanisms, 2) environmental convective available potential energy (CAPE), and 3) strength of the low-level shear. He distinguished among two types of rear inflow: (a) descending rear inflow, and (b) elevated rear inflow. The descending type typifies a decaying mesoscale convective system (MCS), whereby the rear-inflow jet enters the back of the storm at midlevels and descends gradually toward the surface across the stratiform region. This type of structure was produced when CAPE was weak to moderate, and low-level shear was also weak to moderate. The rear inflow was viewed as a horizontal jet driven between two vorticity sources of opposite sign: one derived from gradients in buoyancy above the rear inflow, (i.e., from the warm, backward sloping updraft plume) while the other derived from the thermally direct cool pool circulation. Weisman (1992) documents two cases evolving from maturity to dissipation, and the rear inflow penetrated to the surface approximately 100 and 30 km behind the leading edge. On the other hand, elevated rear inflows produced in Weisman's model results were more typical of stronger, longer-lived systems with strong shear and/or moderate to strong CAPE. The rear inflow remained at several kilometers altitude across the entire stratiform region, plunging to the surface just behind the leading edge.

The present study deals with the structure of a prefrontal wintertime squall line on 13 January 1995 along the U.S. Gulf of Mexico coastal region that developed in the western part of the Gulf during the early morning hours and advanced eastward to the Florida Panhandle later during the day. This line had an extensive trailing stratiform region with qualitative radar features resembling previous squall line conceptual models (Smull and Houze 1987a, etc.), but with noteworthy differences in kinematic structure. The study of this squall line, which occurred in a partly data-sparse region (i.e., over the Gulf of Mexico), was enhanced by the Weather Surveillance Radar-1988 Doppler (WSR-88D) operational radar network and measurements from the downlooking ER-2 Doppler radar (EDOP) on the National Aeronautics and Space Administration (NASA) high-altitude (~20 km) ER-2 instrumented aircraft (Heymsfield et al. 1996a). A unique set of observations from this squall line was obtained with EDOP during a series of ER-2 aircraft flights based out of Houston, Texas, called the Houston Precipitation Experiment (HOPEX), conducted during January 1995. EDOP is an airborne Doppler weather radar system at X band with fixed nadir and

forward pointing beams that map out Doppler winds and reflectivities in the vertical plane along the aircraft motion vector. It provided high-resolution (i.e., 75 m vertical and 200 to 1000 m horizontal depending on altitude) vertical cross sections of reflectivity and Doppler velocity as the ER-2 traversed the stratiform and convective region of this squall line on the outgoing and return flight legs. This emphasis on vertical structure is in contrast to other airborne radars such as ELDORA (Hildebrand et al. 1996) that measure the full three-dimensional structure but with lower vertical resolution. Further details of EDOP are described in the appendix including instrument capabilities, editing steps performed to the observations for analysis and display, accuracies of measurements, and the methodology for computing vertical and horizontal (along the aircraft track) air motions. The WSR-88D radars along the Gulf Coast would not have provided equivalent high vertical resolution information. The squall line was sufficiently far from the radars so that vertical structure would be smeared out by the large radar volumes. In addition, the operational WSR-88D volume scanning with nine elevation steps does not always sample the brightband region and upper-level MCS structure well, due to 1) large elevation steps, 2) not scanning to sufficiently high elevation angles, and 3) inadequate sensitivity at distant ranges.

The purpose of this paper is to present an analysis of the 13 January 1995 squall line with focus on the vertical structure of radar reflectivities and air motions. Specifically, we document the squall line structure, and compare and contrast this structure with other published cases. One unique aspect of the 13 January case is that the rear inflow descends to the surface 200 km behind the leading edge. This provides a flow structure that has two flow regimes: front-to-rear flow overriding a shallow, rear-to-front flow. Typical documented cases have three flow layers, with front-to-rear inflow overriding the rear inflow, and the rear inflow itself overriding lower-level front-to-rear inflow in the stratiform region. Section 2 discusses the overall evolution of the squall line based on WSR-88D measurements and the aircraft flight lines. Since the synoptic-scale forcing is relatively strong on 13 January and presumably plays an important role in the squall line development, section 3 provides the synoptic conditions and also the larger-scale context for later discussion. These analyses show that the north-south squall line orientation is parallel to, and along the edge of, a jet streak, suggesting that the squall line EDOP-measured transverse circulation may be coupled to the larger-scale transverse jet streak circulation. Section 4 examines the vertical structure of the squall line using the EDOP observations. Of particular interest are how the magnitudes of updrafts, downdrafts, and reflectivities, and the overall conceptual structure of this system, compare with those of squall lines in other regions. The microphysical structure of the squall line is examined using the EDOP Doppler

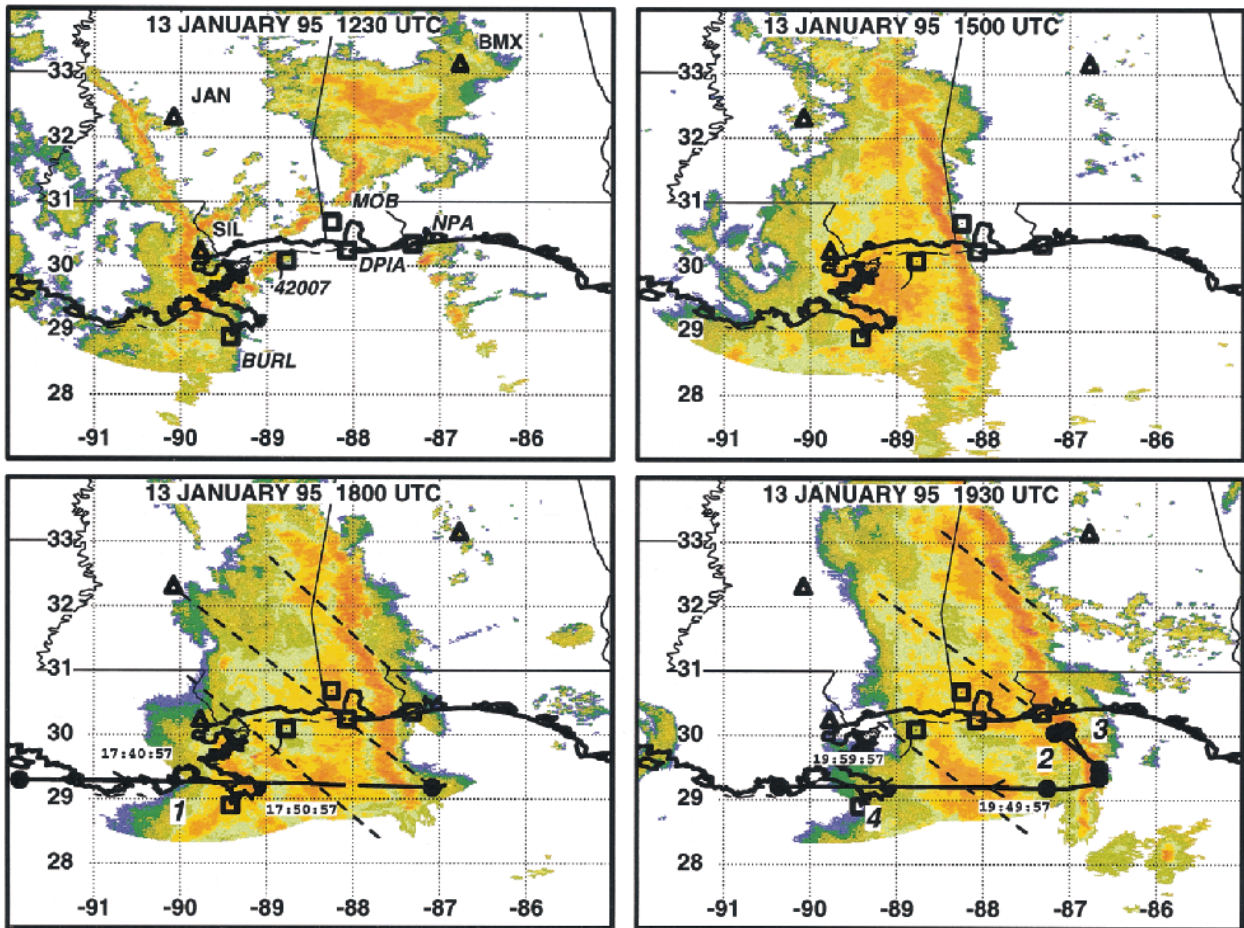


FIG. 1. Radar composite images for squall line along Alabama–Mississippi coastline on 13 Jan 1995 during period 1230–1930. Solid lines indicate positions of ER-2 flight lines at 1730 (line 1 in lower-left panel) and 1922, 1932, and 1940 (2, 3, and 4, respectively, in lower-right panel); arrowheads on lines 1 and 4 indicate direction of travel of aircraft. Locations of upper-air soundings (triangles) and buoys (squares) are shown for all panels and labeled in upper-left panel. Dashed lines in lower panels indicate positions of mesoscale rainbands embedded in stratiform region.

velocities and polarization measurements. Since the squall line has an extensive stratiform region that trails the convective line by a few hundred kilometers, section 4 addresses the sustenance of this stratiform region through EDOP and synoptic observations, the latter of which suggest extensive mesoscale lifting provided by favorable jet streak dynamics. Finally, section 5 concludes by summarizing the general features of this system and its relation of previous studies.

2. General description of squall line

The squall line developed in the western part of the Gulf during the early morning hours and advanced eastward beyond Mobile, Alabama, at the time of the ER-2 overpasses (~ 1800 – 2100 UTC; all times hereafter are in UTC). For illustration of the general structure of the squall line, Fig. 1 shows radar reflectivity composite images from 1230 to 1930 before and during the period of the ER-2 flight tracks. WSR-88D level III gridded

low-level reflectivity (Crum et al. 1993) primarily from Mobile, Alabama (MOB), and Slidell, Louisiana (SIL), were used in this study since the level II volumetric data were not yet routinely recorded from these radars. The precipitation extended well into the Gulf of Mexico in satellite images, although it was beyond the range of the WSR-88D radars.

The WSR-88D radar a few hours prior to 0800 showed numerous weak lines of convection oriented northwest–southeast and an area of disorganized convection near the Louisiana–Alabama border. At approximately 0800, a more intense north–south-oriented line about 200 km in length developed at an approximately 30° angle to the other weak convective lines. This latter squall line remained suppressed until 1200 when pronounced intensification of the maximum reflectivities and growth of convective line heights to near tropopause level occurred. Because of data limitations, it was not possible to determine the origin of strong winds (1140–1240), a possible tornado at about 1100, and a water-

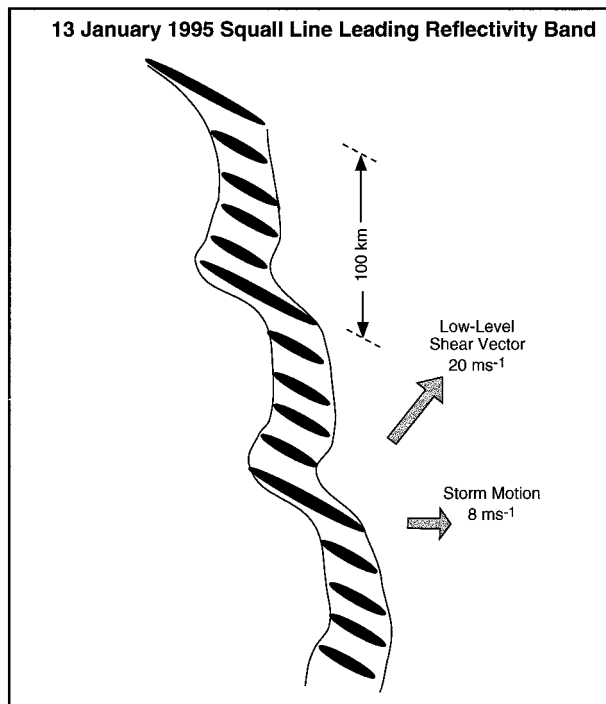


FIG. 2. Schematic of reflectivity band associated with leading squall line convection. Two dominant scales observed are shown.

spout (approximately 1300) reported near New Orleans (near SIL in Fig. 1). These severe weather events occurred near the leading convective line. From about 1400 to 2100, the squall line leading edge reflectivities intensified in a narrow, wavy band roughly 500 km in length. The reflectivities in the leading edge shown schematically in Fig. 2 had enhanced small-scale regions appearing to be composed of short northwest-southeast-oriented convective segments. These segments had similar orientation to the earlier weak convective lines. In addition to these smaller-scale (approximately 20 km) perturbations along the leading edge, there were larger mesoscale (100 km) perturbations along the line (e.g., 1800 panel in Fig. 1). Multiple embedded bands with an oblique orientation relative to storm motion are also documented by Halverson et al. (1999) for a large tropical cloud cluster. Despite the large-scale bowed structure, there were few reports of hail and minimal damage during this more intense convective period.

A stratiform region trailing the convective line began developing after 1300, and it enlarged throughout the intensification and dissipation of the convective portion. The dissipation of the whole system began after about 2000, evidenced by the weakening of both the leading edge radar reflectivities from the portion of the squall line over the Gulf of Mexico, and decaying of the overall stratiform region. The squall line segment over land farther to the north continued to persist beyond 0000 on 14 January. The eastward motion of the squall line varied from about 9 to 10 m s^{-1} early in the lifetime,

then slowed to about 7 m s^{-1} after approximately 2000. The total rainfall associated with the entire squall line passage (convective and stratiform regions) from 1600 to 2200 at MOB and a few other stations was about 25 mm.

Throughout the mature period of the squall line, a reflectivity minimum with a width of about 20 km was present immediately to the rear of the convective line. These radar reflectivity minima at low- to midlevels are a common feature of squall line systems (Houze 1977; Smull and Houze 1987a; Biggerstaff and Houze 1991). Biggerstaff and Houze (1991) hypothesized that the reflectivity trough for the Preliminary Regional Experiment for the Stormscale Operational and Research Meteorology Program (PRE-STORM) 10–11 June 1985 case resulted from microphysical processes (i.e., fall speed sorting of hydrometeors) and dynamical causes (i.e., deep subsidence).

3. Synoptic and mesoscale environments during squall line development

a. Coupling of the synoptic flow with squall line

The squall line development appears to be coupled with the larger-scale environment as described in the following section. An upper-level trough of low pressure at 0000 on 13 January, combined with warm moist advection in low layers from the Gulf of Mexico, provided for favorable severe weather conditions along the coastal region. Figure 3 shows the surface, 700-mb, and 300-mb conditions for 0000, 1200, and 1800 on 13 January 1995 and 0000 on 14 January 1995. Superimposed on the surface charts are the 0.5° radar echo composites near the surface level as obtained from the WSR-88D radars. Heights and isobars in the figure were obtained from the GEMPAK objective analysis software using the Barnes algorithm (Koch et al. 1983). Because upper-air data are nonexistent over the Gulf of Mexico, the 700- and 300-mb analyses with the exception of the 1800 panel were obtained from the National Center for Atmospheric Research (NCAR) archived, Nested Grid Model (NGM) model initialization dataset (190.5-km resolution) that incorporates all available conventional observations and provides consistent analyses over the data-void region. The 300-mb analysis at 1800 uses the 6-h NGM forecast at 1200. Comparisons of major features in the objectively analyzed upper-air data over land were qualitatively consistent with the NGM analyses, and the salient synoptic features are represented adequately in Fig. 3.

The surface analyses show a cold front along the eastern Texas border, a low with a 999-mb minimum at 1800 located in Arkansas, and a stationary front extending to the northeast. The squall line located near SIL in Fig. 3 (0000 14 January) is roughly centered on the positions of cross sections presented later and it is located well ahead of the surface cold front. By 1200 on 14 January (not shown), the cold front nearly ad-

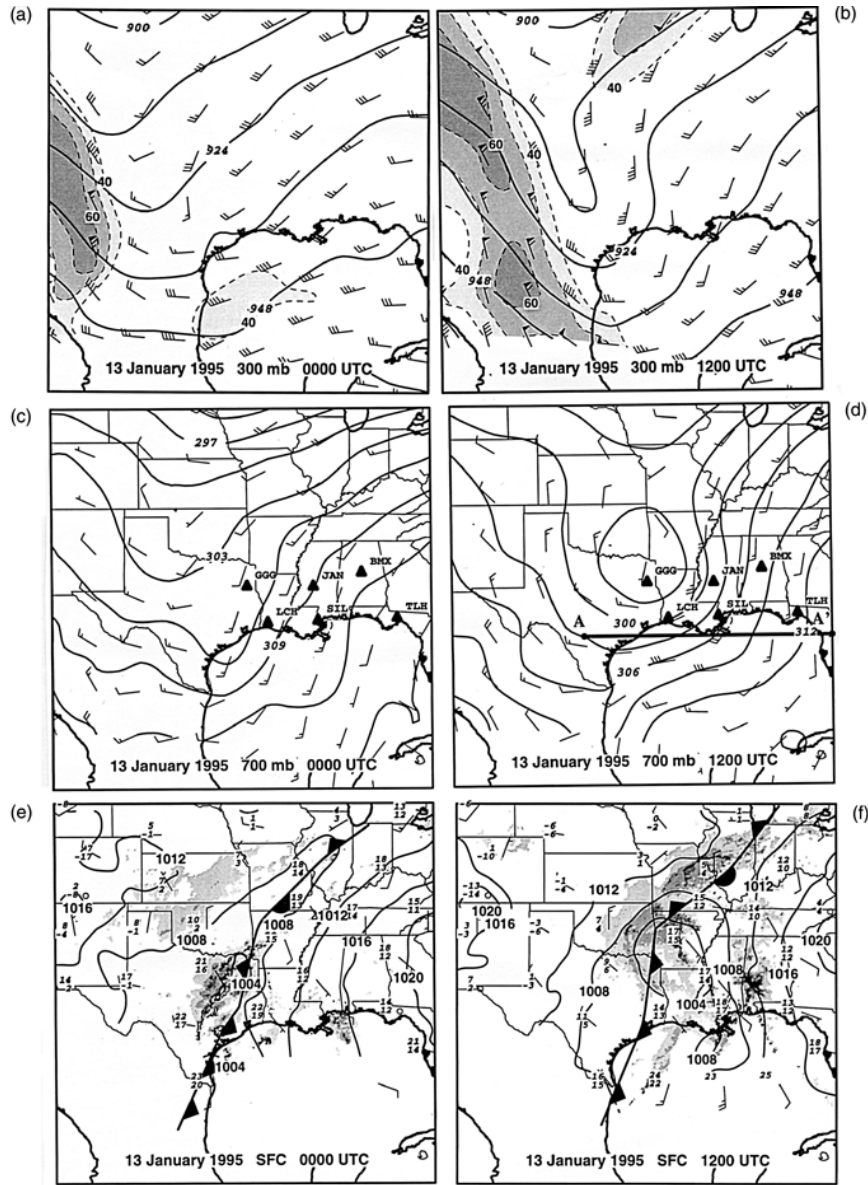


FIG. 3. Analysis maps for 13 Jan 1995 (0000, 1200, 1800 UTC) and 14 Jan (0000 UTC). Surface analyses were obtained from objectively analyzed surface data; 700- and 300-mb data were from NGM initialization (0-h forecast) except for 13 Jan at 1800, which uses the 6-h forecast from 1200. WSR-88D radar composite images at map times and surface fronts are superimposed on surface maps. Solid contours are isobars in 4-mb increments (surface) and heights in 3-dm (12-dm) increments for 700 (300) mb. Isotach (dashed contours) at 300 mb are in 10 m s⁻¹ intervals. Full wind barb = 10 m s⁻¹, and a solid pennant = 50 m s⁻¹. Positions of vertical cross sections (Fig. 4), and location of relevant upper-air soundings are shown at 700-mb level.

vanced into the Florida Panhandle and caught up with the leading edge of the rain.

The squall line developed east of an intensifying trough, as indicated by the 300- and 700-mb analyses. The intensification of the trough is clearly evident in the sequence of 700-mb analyses in Fig. 3. After 0000 on 13 January, the height field formed a closed circulation with a minimum of about 2060 m at 1200, and further decreased to 2010 m at 0000 on 14 January. The

300-mb analyses show embedded jet streaks exceeding 60 m s⁻¹ on the western side of the trough. The importance of jet streak dynamics to the development of severe weather events has been discussed by Uccellini and Johnson (1979) and others. They suggested that transverse vertical circulations associated with upper-level jet streaks can establish favorable large-scale environments (i.e., strong upper-level diffluence, strong low-level vertical shear, and strong instability) for

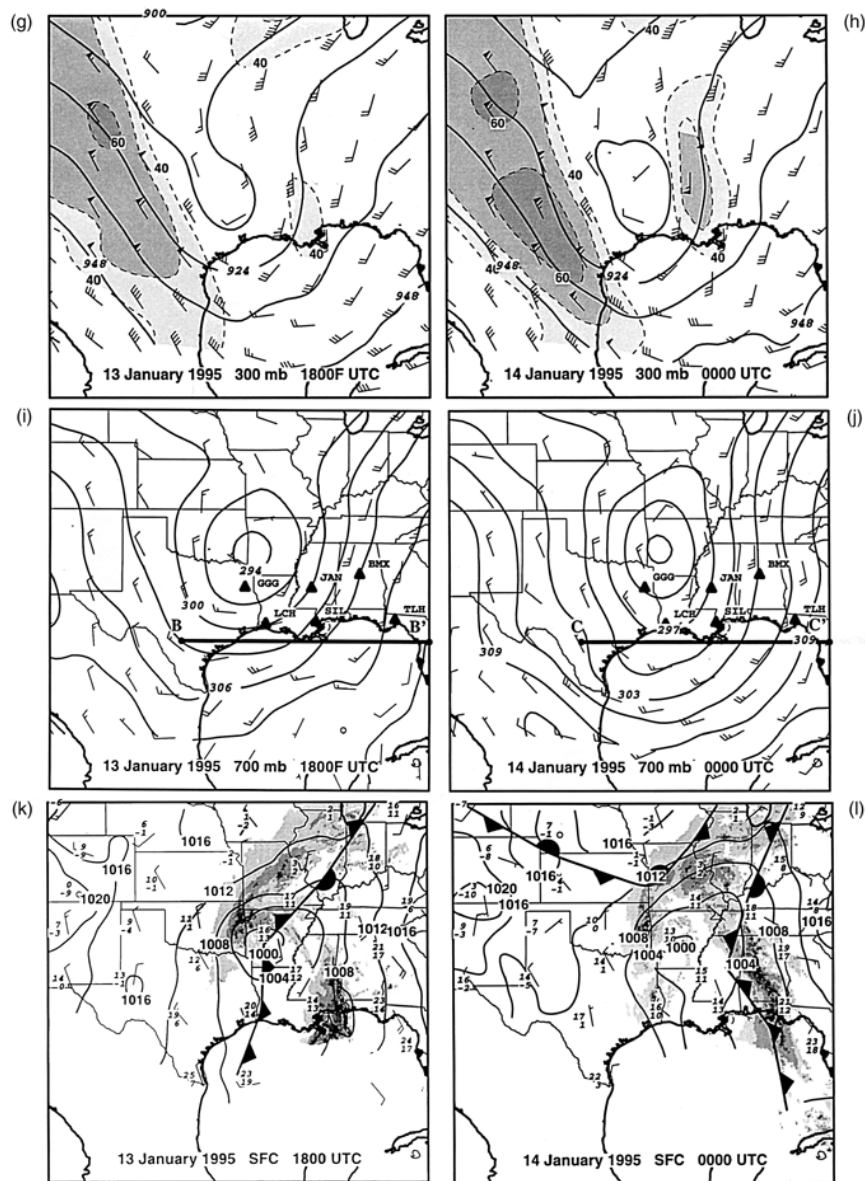


FIG. 3 (Continued)

strong, deep convection. The reflectivities associated with the squall line convective leading edge intensified between 1200 and 1800, and they coincide with the development of a 40 m s^{-1} jet maximum on the eastern side of the trough and to the rear of the squall line leading edge. At 1800, the squall line was located within the right-rear quadrant of the jet maximum and it was embedded in diffluent flow (labeled A in Fig. 3). By 0000 on 14 January, this jet maximum advected around the jet axis (northward) and exceeded 50 m s^{-1} . The north-south-oriented squall line lies along the eastern edge of the similarly oriented jet streak. Whether this wind maximum is due to a jet streak advecting around the base of the trough, from intensification of the trough, or from the convective system feedback on the larger-

scale environment, cannot be ascertained. The 300-mb NGM analysis at 1200 does not show evidence of a jet streak propagating around the trough; the analysis may have missed any jet streaks over the Gulf of Mexico since there are no soundings on which to base the analysis. Equally plausible, however, is that the jet maximum intensified at 300 mb as the trough deepened and became cutoff.

To elaborate more on the synoptic environment during the squall line development, Fig. 4 shows east-west vertical cross sections at 1200 (AA') and 1800 (BB') on 13 January, and 0000 (CC') on 14 January for (a) meridional storm-relative wind speed (v_{rel}) and relative humidity contours with superimposed observed wind vectors, and (b) vertical velocity (ω) and potential vor-

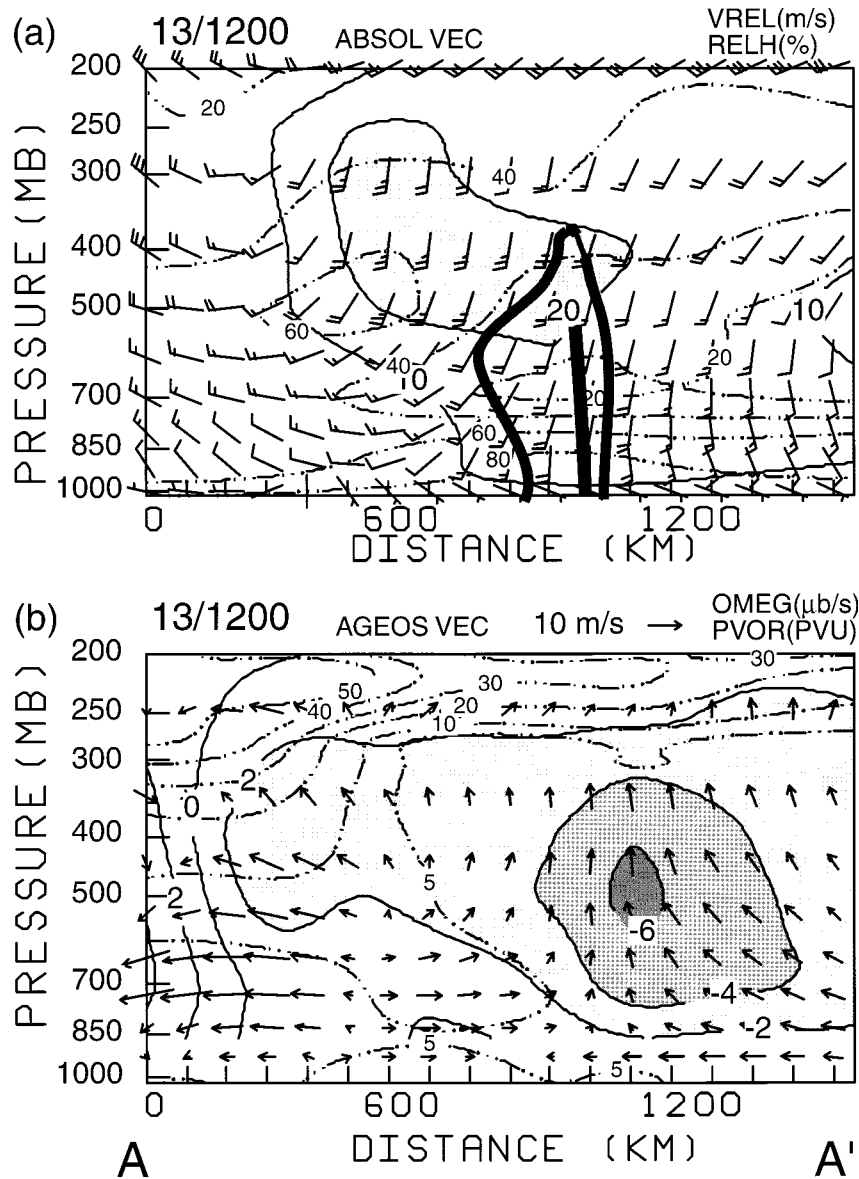


FIG. 4. Vertical east-west cross sections AA', BB', and CC' whose respective positions are shown in Fig. 3 at 1200 and 1800 on 13 Jan, and 0000 on 14 January. Section BB' uses the 6-h NGM forecast from 1200 UTC on 13 January; the other sections use the upper-air observations. (top) Absolute wind vectors with meridional relative wind speed (v_{rel}) contours for values $>10 \text{ m s}^{-1}$ and in 10 m s^{-1} intervals (solid curves), and RELH in 20% intervals (dotted-dashed). NGM output was only available up to 300 mb at 1800. (bottom) Ageostrophic wind vectors (in plane of cross-section) with vertical velocity ω in $2 \times 10^{-3} \text{ mb s}^{-1}$ intervals (solid contours), and potential vorticity (PVOR) in 10 PVU ($=10^{-6} \text{ m}^2 \text{ s}^{-1} \text{ K kg}^{-1}$) intervals except a 5-PVU contour added (dotted-dashed). (PVOR omitted for forecast in section BB'.) Locations of upper-air stations at GGG, JAN, BMX, LCH, SIL, and TLH are shown in 700-mb panel. The squall line radar echo derived from EDOP is outlined on cross sections. Bold vector on sections BB' and CC' show rear intrusion into squall line.

ticity contours with ageostrophic wind vectors in the plane of the cross section. The position of these cross sections are shown in Fig. 3. Locations of upper-air stations at Gage, Oklahoma (GGG); Jackson, Mississippi (JAN); Birmingham, Alabama (BMX); Lake Charles, Louisiana (LCH); Slidell, Louisiana; and Tal-

lahassee, Florida (TLH) are shown in the 700-mb panel. They approximately bisect and are roughly perpendicular to the squall line. Similar to Fig. 3, the 1800 time uses the 6-h NGM forecast for 1200, while the other times use objectively analyzed upper-air data. Note that except for the 1800 time, all parameters were obtained

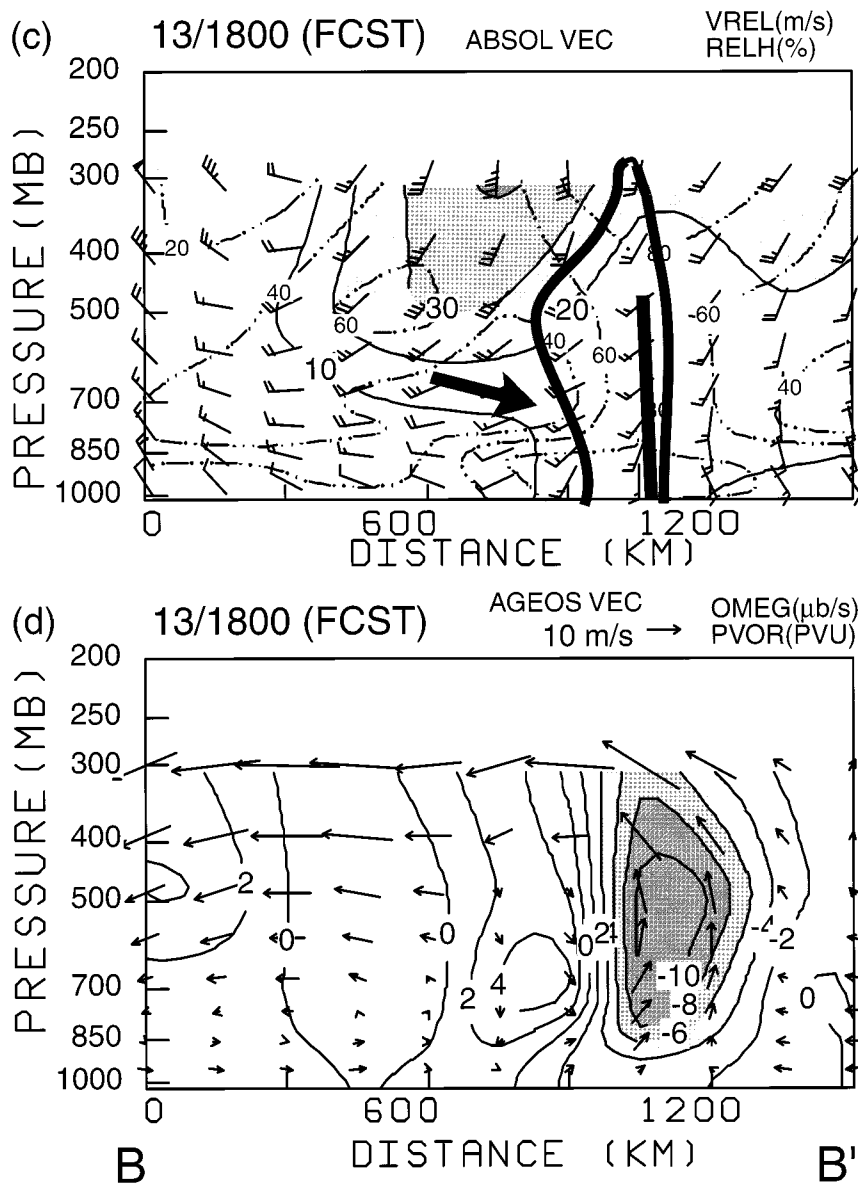


FIG. 4 (Continued)

from the objectively analyzed upper-air data; $\omega = dp/dt$ was calculated from the GEMPAK variational adjustment routines. Unfortunately, the NCAR-archived NGM model runs for this study were available only up to the 300-mb level and are of coarse resolution, so diagnostic calculations were not attempted. Thus, for the 1800 time, potential vorticity was not calculated and meridional winds are not shown above 300 mb. The ageostrophic winds were calculated from the model and objectively analyzed height fields. The approximate outline of the radar echo associated with the squall line (based on the EDOP 5-dBZ reflectivity contour for line 1) is shown in sections AA', BB', and CC'.

The cross sections in Fig. 4 provide the larger-scale context for later discussion of the airborne radar ob-

servations. All three cross sections indicate strong upward motions in the vicinity of the squall line, with values ranging from about $-6 \times 10^{-3} \text{ mb s}^{-1}$ at 1200 to $-10 \times 10^{-3} \text{ mb s}^{-1}$ at 0000. Subsidence is noted to the rear of the squall line at 1800 with $4 \times 10^{-3} \text{ mb s}^{-1}$ descent at 700 mb. The NGM ω forecast at 1800 slightly leads the convective line, providing favorable lifting in the environment ahead of the squall line, enhancing squall line propagation to the east. The jet stream maximum intensifies from 20 m s^{-1} at 1200 to 40 m s^{-1} at 0000, and the flow is generally parallel to the line (i.e., into the page) throughout much of the troposphere. Potential vorticity, which can be useful for depicting tropopause folds, indicates the existence of such a fold at 0000. Also evident in the potential vor-

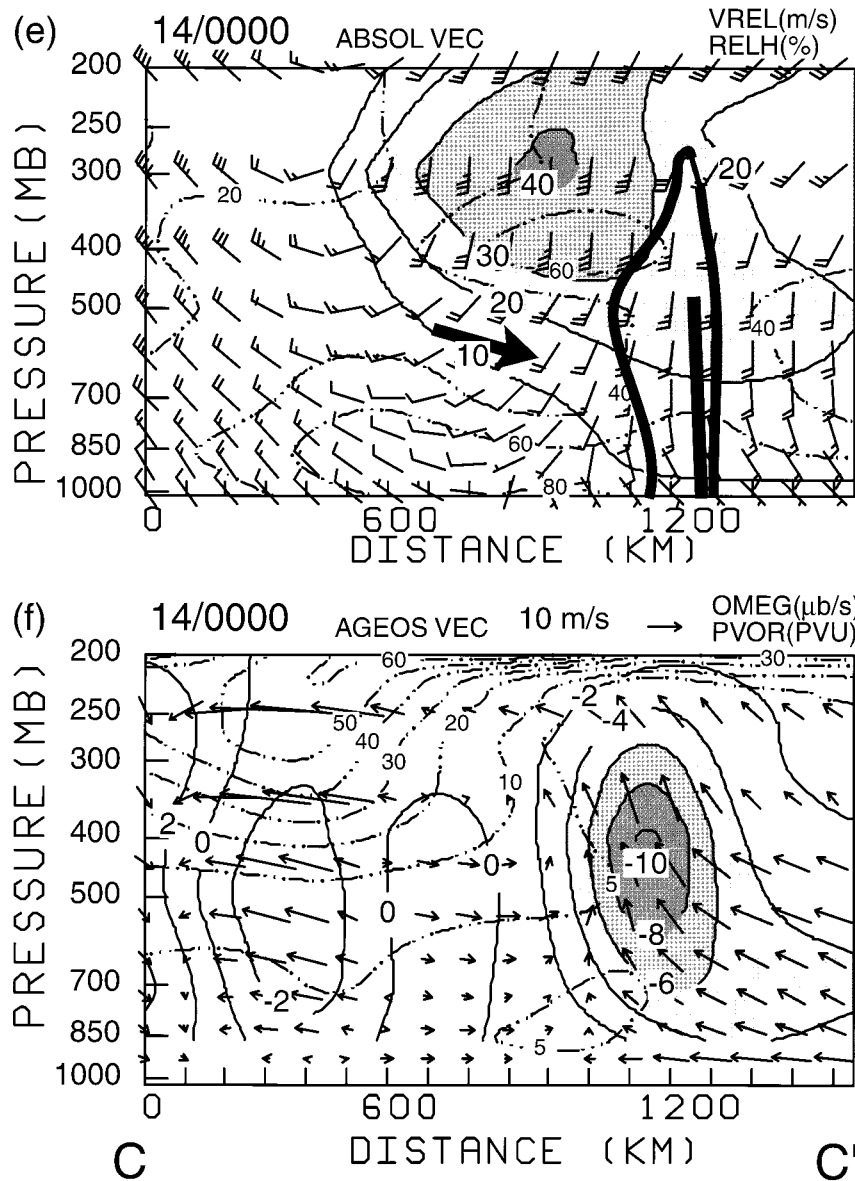


FIG. 4 (Continued)

tivity is a lowering of the tropopause from 12-km altitude ahead of the line to about 9-km altitude to the west. Coinciding with this fold is a pronounced dry air intrusion into the rear of the squall line system in the midlevel relative humidities at 1800 and 0000. The ageostrophic wind vectors along with the above discussion support the idea that the larger jet dynamics established a mesoscale thermally direct vertical circulation across the transverse plane of the squall line. A strong vertical motion couplet is set up with ascending air slightly ahead of the squall line, and strong subsidence to the rear of the squall line. Note that the surface cold front is poorly defined at this time and it is located well to the west of the squall line.

b. Near-squall line environmental conditions

The upper-air soundings (Fig. 5) ahead of and behind the squall line indicate several important aspects of the squall line environment. The large (~400 km) spatial separation of upper-air soundings, 12-h temporal sampling, and prior convective activity, required care in choosing a representative sounding ahead of and behind the squall line. Furthermore, the soundings were all north of the aircraft flight lines (see Fig. 4 at 700 mb). It was concluded that the most representative conditions ahead of the line were given by soundings from JAN and SIL at 1200, whereas the LCH (0000 on 14 January) and SIL (0000 on 13 January) soundings were most

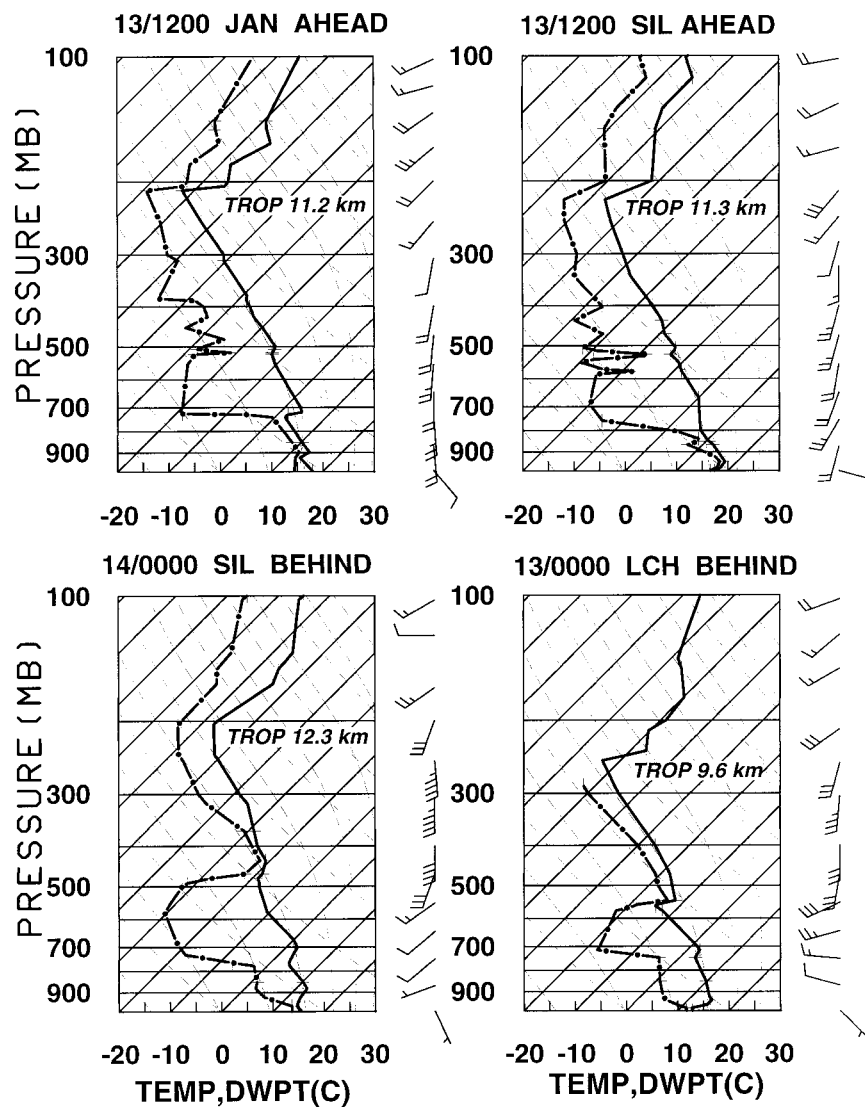


FIG. 5. Upper-air soundings ahead of squall line at 1200 on 13 Jan (JAN and SIL), and behind squall line (SIL at 0000 on 14 Jan) and LCH at 0000 on 13 Jan). Standard skew T diagram provides temperature (bold solid), dewpoint temperature (bold dotted-dashed), adiabats (dashed), and pseudoadiabats (thin dotted-dotted). Whole wind barb = 10 m s⁻¹; half wind barb = 5 m s⁻¹.

representative of conditions *behind* the leading squall line edge. These wake soundings are located in the dry, midlevel air to the rear of both the convective and stratiform regions. Moisture inflow into the squall line is shallow as evidenced in the SIL sounding by high dewpoints below 1.5 km and strong directional shear in the shallow layer below 900 mb. The tropopause height shows a marked lowering from ~ 11.2 km altitude ahead (JAN, 1200; SIL, 1200) to ~ 9.6 km well to the rear of the line (LCH, 0000 on 13 January). The post-squall line soundings also show midlevel moisture associated with trailing anvil cirrus and nimbostratus, above the dry intrusions at SIL (0000 on 14 January) and LCH (0000 on 13 January). The intrusion has dry-adiabatic lapse rates due to synoptic-scale subsidence. Also, evap-

orative cooling below cloud base on the mesoscale contributes to steepening of the lapse rate beneath the anvil. The trailing cirrus extends well west (~ 500 km) of the leading edge of the squall line, as observed with both visible and IR satellite measurements.

The pre-squall line soundings had unexpectedly low values of CAPE. The squall line passage was at about 1400 at JAN and the 1200 JAN sounding had a CAPE of only 11 J kg⁻¹, whereas the SIL 1200 sounding, which was slightly ahead of the squall line, had a CAPE of 831 J kg⁻¹. The LCH sounding at 0000 on 13 January (not shown) had the highest prestorm CAPE of 1288 J kg⁻¹; all the other available soundings had near-zero CAPE. There are a few possible explanations for the low CAPEs observed. The CAPEs were calculated using

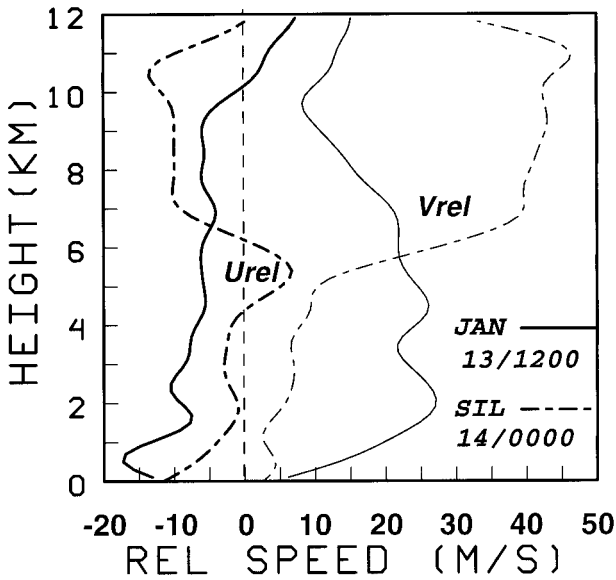


FIG. 6. Storm-relative winds from ahead of line (JAN at 1200 on 13 Jan 1995) and behind line (SIL at on 14 Jan 1995).

parcel properties averaged over the lowest 500 m. Only early morning 1200 soundings were available and CAPEs may be higher if soundings are modified by daytime heating. But there is fairly widespread cloud cover out ahead of the squall line, and surface stations do not show appreciable warming during the morning. In addition, there were prior lines of weak convection and stratiform rain that may have stabilized the environment. Thus we have not modified these soundings since these other factors have an unknown effect on the pre-squall line boundary layer. Development of the squall line in a low CAPE environment would require strong dynamical forcing. Such was the case with the severe squall study by Carbone (1982) in which he concluded that squall line circulation probably resulted from gravity current forcing since CAPE was negligible in the nearby soundings. In the present case, in addition to the instability of the environment, the squall line development and sustenance appears to be coupled with mesoscale jet streak dynamics.

Vertical profiles of squall line–relative zonal (u_{rel}) and longitudinal (v_{rel}) wind components corresponding to the soundings in Fig. 5 are provided in Fig. 6. As recalled, squall line motion is due east between 7 and 10 $m s^{-1}$ with a mean of about 8 $m s^{-1}$ and thus 8 $m s^{-1}$ has been subtracted from the u component to form u_{rel} . Several features are noted in the figure: 1) as also shown earlier in the vertical cross sections, u_{rel} from 0 to 6 km has decreased about 5 $m s^{-1}$ between the pre- and post-squall line soundings (Fig. 4); 2) the pre-squall line inflow is evidenced by a strong alongline shear layer between the surface and 2-km altitude, with easterly flow ($u_{rel} \sim -17 m s^{-1}$); 3) relative flow behind the line between 4- and 6-km altitude becomes positive

($u_{rel} \sim 5 m s^{-1}$), that is, rear inflow; and 4) the presence of the intensifying jet streak is evident by an increase in the upper-level southerly flow (v_{rel}) between 6- and 11-km altitude. The surface to 6 km layer and the surface to 2 km layer shears for the pre-squall line sounding are $4.9 \times 10^{-3} s^{-1}$ toward 25° and $1.0 \times 10^{-3} s^{-1}$ toward 65° . Based on other available soundings ahead of the line, the density-weighted shear vector from the surface to 6 km altitude is oriented at $\sim 50^\circ$ oblique angle to the squall line. This type of squall line therefore falls between shear parallel and shear perpendicular. Figure 2 also shows how the low-level shear vector is oriented perpendicular to small-scale convective segments in the leading line. Similar orientation of tropical convective lines with respect to the surface to 2 km shear vector has been reported by LeMone et al. (1998). Rotunno et al. (1988) concluded from model simulations that lines of supercells formed with strong, deep shear oriented at an angle to the line, whereas lines with ordinary evolving cells formed with strong shear at low levels directed perpendicular to the line and with weak shear aloft. The wind shear for the present case suggests a different combination of shear attributes, that is, very shallow shear oriented at an angle to the line.

4. Squall line structure from EDOP observations

a. EDOP-derived vertical reflectivity structure

The ER-2 performed four main flight tracks that were useful for study of the squall line structure. The locations of these flight lines are plotted in Fig. 1 and consist of two long (~ 350 km in length), roughly squall line–perpendicular tracks in transit to and from the squall line (hereafter called lines 1 and 4), and two short (~ 80 km long) line-parallel tracks (called lines 2 and 3). Line 1 (1730–1807) is eastward and line 4 (1940–2008) is westward almost along the same latitude but nearly 2 h later; these lines will be the focus of this paper. On the return flight line (line 4), the aircraft turned over the leading convective region and thus did not provide good coverage of the convection. Lines 2 and 3 were oriented from southeast to northwest and northwest to southeast, respectively.

Figure 7 shows reflectivities for flight lines 1 and 4. Line 1 (Fig. 7a) provided coverage of the entire width of the squall line, which shows a leading convective region at about 450-km distance with tops extending to 11.5 km and peak reflectivities of about 55 dBZ. An extensive stratiform region over 200 km in width is evident with two regions of enhanced reflectivity between 200- and 250-km distance, and 300- and 400-km distance, respectively. This stratiform region is somewhat larger than typically observed for squall lines (e.g., Smull and Houze 1987a). A well-defined bright band covers the entire width of the stratiform region with peak reflectivities near 50 dBZ in the enhanced strati-

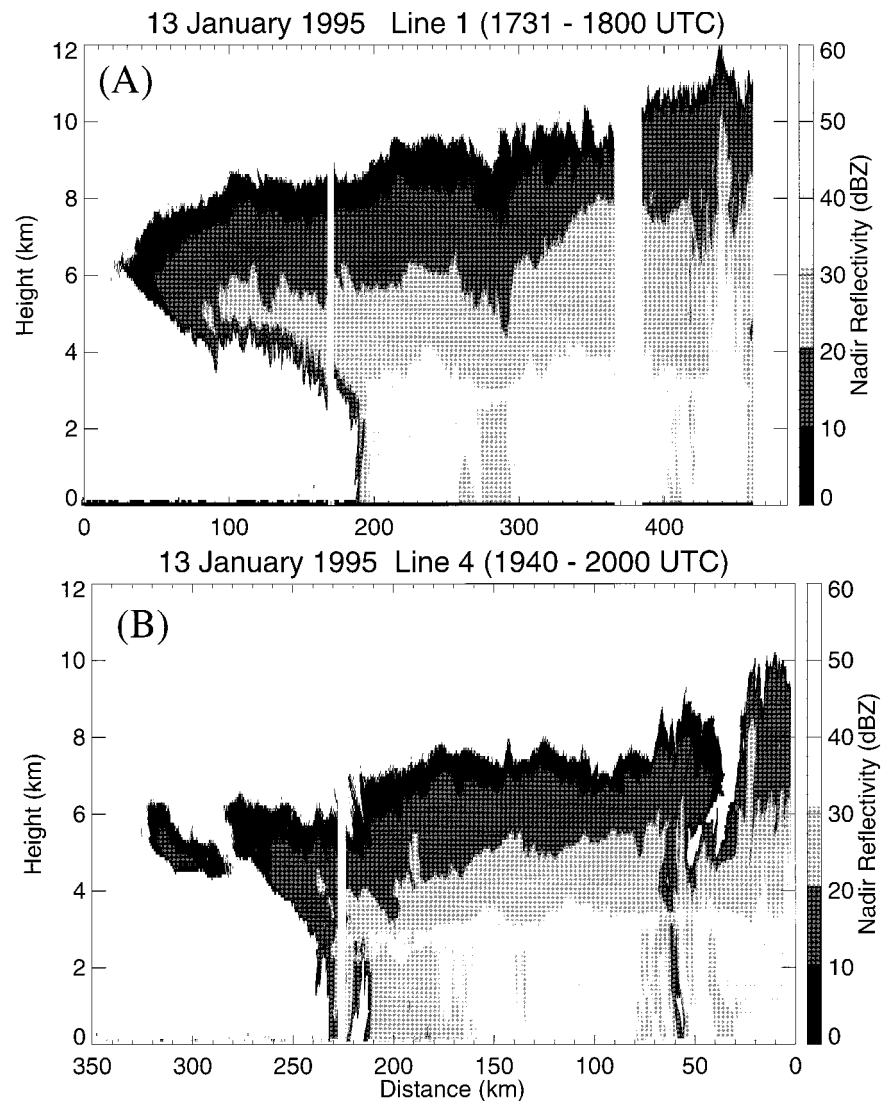


FIG. 7. Vertical cross sections of EDOP nadir reflectivity for flight lines 1 (top) and 4 (bottom). Locations of cross sections are shown by lines 1 and 4 in Fig. 1. Aircraft is traveling from left to right in top panel, and right to left in bottom panel.

form regions. The stratiform rain region ends at about 180-km distance, and an elevated anvil between 4- and 9-km altitude trails the stratiform region. Line 4 (Fig. 7b) reveals a lowering of the stratiform region cloud top by about 2 km and a weakening of the convective line. Enhanced reflectivity regions still exist, although they have moved relative to the convective region. Also, the transition region becomes better defined with a major collapse of the cloud top between 30 and 40 km behind the leading edge.

b. Mesoscale structure of stratiform and convective regions

Figure 8 presents EDOP nadir reflectivity, hydrometeor velocity, vertical motion w , and squall line-rel-

ative zonal wind $u_r = u - V_s$ ($V_s = 8 \text{ m s}^{-1}$) for the stratiform and convective section of flight line 1. The hydrometeor velocity is the measured Doppler velocity corrected for aircraft motions; the w and u_r components were derived from the nadir Doppler velocities with the assumption of hydrometeor fall speed relations (see the appendix). In addition, the calculated u_r and w panels have been smoothed horizontally with a heavy running average filter (101 points, which is equivalent to a 10-km scale length) in order to accentuate the broader-scale stratiform vertical and horizontal winds; later the unsmoothed w in the convective region will be presented. Also superimposed on Fig. 8 are relative humidity (RELH), zonal (UREL), and longitudinal (VREL) winds, and ω (OMEGA) contours interpolated from the 1200 NGM 6-h forecast grid. Although these contours

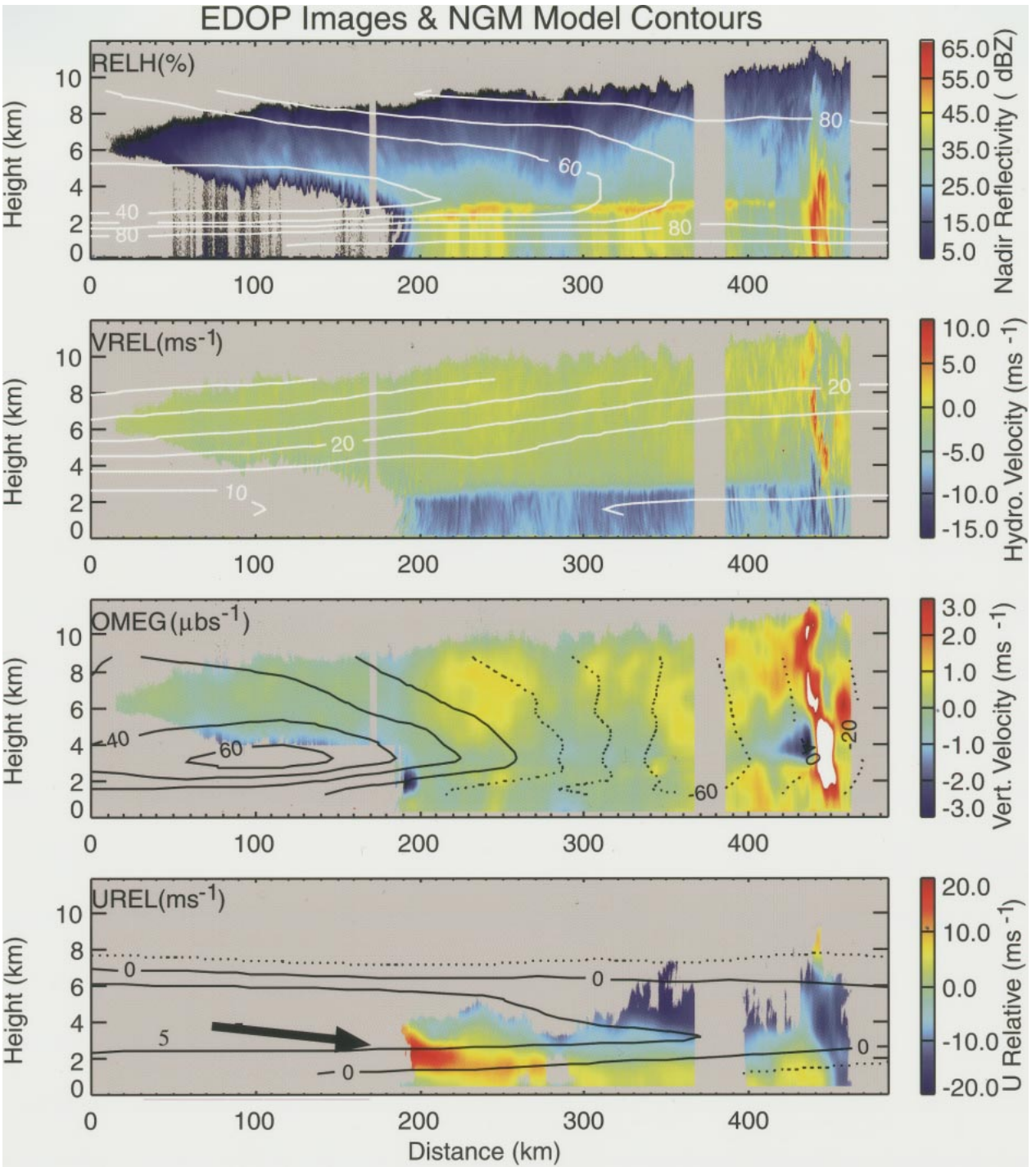


FIG. 8. EDOP flight line 1 (1730–1807) data with registered National Centers for Environmental Prediction (NCEP) 1800 forecast contours superimposed. Shown from top to bottom are nadir reflectivity, vertical hydrometeor velocity, vertical velocity, and horizontal (alongtrack) winds. Position of this cross section (shown in Fig. 1) is oriented with west on the left side of the figure and time increasing from left to right. Gap in data at about 370 km is due to closing of a data file during flight. Contoured NCEP forecast from top to bottom are relative humidity (RELH), v_{rel} (VREL), ω (OMEG), and v_{rel} (UREL); dashed contours are negative. White area in vertical velocity panel denotes values greater than 3 m s^{-1} . See text for details.

are roughly matched in time, errors in alignment are due to inadequacies in the forecast.

As with the reflectivity characteristics of the squall line shown earlier (Fig. 1), the hydrometeor and vertical velocities clearly depict the convective and stratiform regions of the squall line. Due to the difference in fall speeds between snow and rain, hydrometeor velocities in the stratiform region (between 200- and 420-km distance) increase from 1 to 2 m s⁻¹ in the snow layer above the melting level, to greater than 6 m s⁻¹ in the rain layer below the bright band. Although not obvious in this broad-scale presentation, there are many fall streaks with typical dimensions of 1 to 2 km embedded in the stratiform rain region.

The w panel in Fig. 8 shows a number of important aspects of the squall line. A strong rearward-tilted updraft is evident in the convective region (400- and 450-km distance), and two enhanced regions (at ~210–260-km distance and ~300–360-km distance) of lifting of 1–2 m s⁻¹ are present between 4 and 8 km in the stratiform region. The enhanced regions of upward vertical motions in the stratiform region coincide with regions of higher reflectivities in the bright bands. Based on analysis of the WSR-88D radar echoes such as in Fig. 1, these enhanced reflectivity and vertical motions regions correspond to rainbands separated by about 100 km. These bands of similar spacing existed prior to the development of the squall line stratiform region, but later were found embedded in the squall line stratiform region during the aircraft overflights. Given that the prior weak rainbands present in the WSR-88D radar observations and EDOP-observed stratiform bands had similar 100-km spacings, there is suggestion that gravity waves coexist with the squall line; however, surface observations did not have sufficient spatial or temporal coverage to verify this contention. The magnitude of the stratiform motions are somewhat larger than have been observed previously in squall line studies (e.g., Rutledge et al. 1988); the magnitudes of the vertical motions will be elaborated on in subsequent discussion.

The u_r panel shows squall line–relative zonal winds only in the higher reflectivity rain region, since EDOP's forward Doppler channel was noisy due to microwave leakage in the receiver (see the appendix). A strong rear-inflow jet from west to east is seen to undercut the entire stratiform region. This rear-inflow jet appears to plunge to the surface at the rear edge of the stratiform region (~280 km distance) and diverges forward from this point. The surface observations (not shown) are consistent with this rear inflow. Above this rear inflow, the EDOP-derived squall line–relative zonal winds show flow from front to rear with magnitudes of about 10 m s⁻¹. The mesoscale NGM-derived contours in Fig. 8 are consistent with the EDOP observations, but with some exceptions. A mesoscale current on the trailing edge of the stratiform region is evident by low relative humidities and strong descent ($\omega \sim -50 \times 10^{-3}$ mb s⁻¹). This also occurs on the left flank of the jet stream with

VREL of 35 m s⁻¹ above the rear edge of the stratiform region. There are several important differences, however, between the NGM contoured overlay and higher-resolution EDOP measurements. The NGM 6-h forecast vertical velocities lag the actual EDOP observations, and UREL does not descend to the surface behind the rear edge of the stratiform region. Considering the coarseness of the model and the limitations of the NGM dataset available, the NGM output can only be used here for general interpretations. Our intent here is to show overall similarity in the transverse jet streak circulation and the EDOP-measured storm internal circulation. Unfortunately, none of the available soundings were taken within the stratiform region of the squall line to confirm this EDOP-derived flow field.

Several other factors are noteworthy in the squall line zonal flow field. The reflectivities on the rear edge of the stratiform region indicate a pronounced bright band centered near the 0° isotherm (~3 km altitude) west of the convective region (~225 km distance) where it undergoes an abrupt discontinuity and lowering by about 400 m. This suggests the 0° isotherm lowers abruptly to the west of this point as a result of evaporative cooling. Snow falling from the anvil into the dry subsiding rear inflow will produce cooling. This evaporative cooling will result in a lowering of the melting level. Interestingly, precipitation streamers at the rear edge of the stratiform region (Fig. 8) also showed evidence of evaporation. The bright band in line 4 (Fig. 7) that occurred nearly 2 h later also lowers on the rear edge of the stratiform (180 km in Fig. 7), again suggesting a persistent lowering of the 0° isotherm. The soundings (Fig. 5) also support this contention since they indicate a lowering of the 0° isotherm from 680 mb ahead of the line in the 1200 SIL sounding to 780 mb well to the west of the line in the 0000 LCH sounding (see Fig. 5). The coincident brightband discontinuity and rear-inflow descent also correspond roughly to the rear edge of a mesohigh in the surface observations (not shown).

For comparison with stratiform regions in previous studies, Fig. 9 presents contour frequency by altitude diagrams (CFADs) described by Yuter and Houze (1995) for the stratiform region in Fig. 8 for reflectivity, fall speed, w , and u . These plots, which are essentially two-dimensional histograms, are constructed from one-dimensional histograms over each vertical level (0.75-m intervals) with appropriate normalization described by Yuter and Houze. Differences between the mean values and the maxima of the CFAD contours indicates a skewed distribution at a particular height. The CFAD of nadir reflectivity shows the reflectivity maxima in the bright band are between 35 and 50 dBZ, which are quite large for stratiform regions (e.g., Yuter and Houze report values of 30–42 dBZ in the 11 June 1985 PRE-STORM case). The rain layer reflectivities are also quite high with mean values of about 38 dBZ and a range of values from about 28 to 45 dBZ. The CFAD for reflectivities in the transition region (not shown) showed a similar

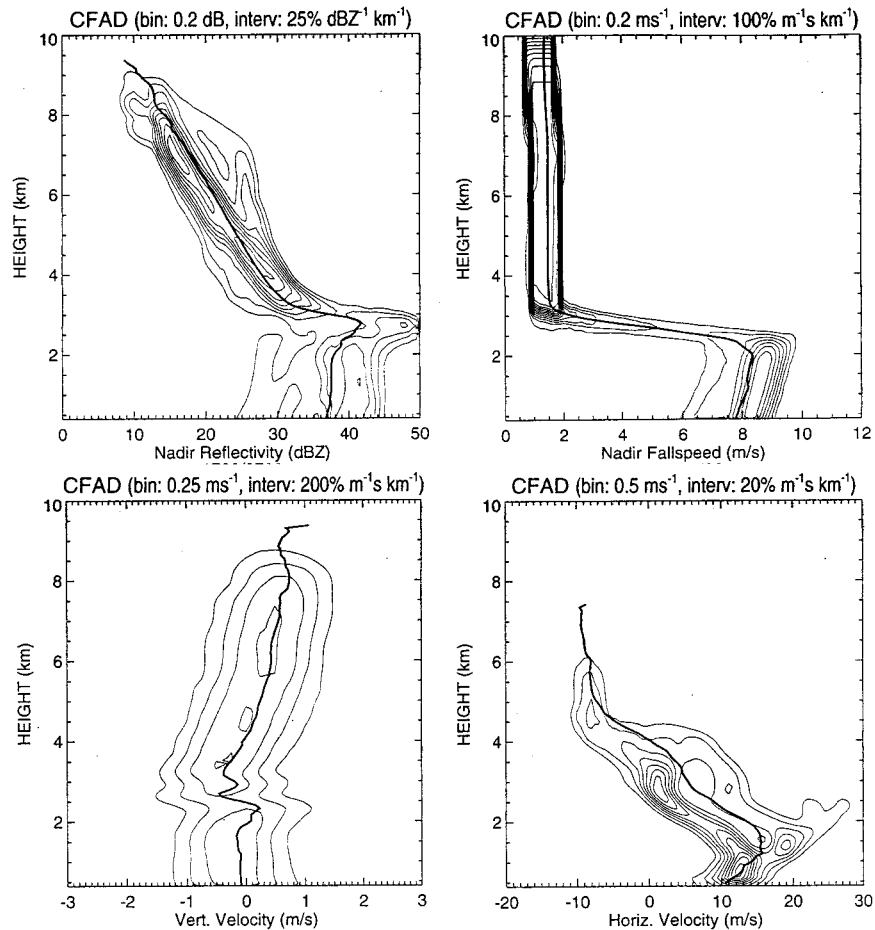


FIG. 9. Contoured frequency by altitude diagrams in the stratiform region (180 to 380 km in Fig. 8) for reflectivity, vertical hydrometeor velocity, vertical velocity w , and horizontal velocity u . Contour intervals and bin sizes are shown in each panel; outer contour value is that given by the interval. The solid curves are obtained from the mean values at each gate.

profile except that the mean rain layer reflectivity was lower by about 6 dBZ. The fall speeds calculated from Eqs. (A1)–(A3) in the appendix range from about 7 m s^{-1} in the rain layer to 1 m s^{-1} in the snow region. The rain layer fall speeds are large but not surprising in view of the high reflectivities. These values are consistent with those reported by Rutledge et al. (1988). Presumably, the rapid increase in fall speeds from above to below the melting layer is due to aggregation of snowflakes that subsequently melt into large raindrops. Below the bright band, the decrease in mean fall speed toward the surface is due to a combination of the density dependence term given in Eq. (A1), rain evaporation, and collisional breakup. These effects will all contribute to a decrease of the mean reflectivity and fall speed with decreasing altitude. The latter two effects have been described in detail in the literature (e.g., Pruppacher and Klett 1997).

The vertical velocity CFAD shows the mean vertical motions in the stratiform region gradually increase above 4-km altitude to about 1 m s^{-1} between 7- and

9-km altitude. This implies that the stratiform rain is produced at higher levels in the stratiform region by fairly substantial lifting. Note that the vertical velocity is inaccurate in the melting layer region because of the difficulty in estimating the fall speeds in this transition region. Thus, vertical velocity values in the 2–3-km-altitude region should be interpreted with caution. The downdrafts in the rain region below about 2-km altitude are less than a few tenths of a meter per second, which is below the accuracy expected from the averaged EDOP observations. Errors arise from the rain fall speeds (see the appendix) used to correct the hydrometeor motions that have uncertainties due to the raindrop size distribution. Biggerstaff and Houze (1991) found from the PRE-STORM 10–11 June 1985 case that both the mesoscale updraft at upper levels and mesoscale downdraft at low to midlevels were on the scale of the trailing stratiform precipitation. For this case, Rutledge et al. (1988) found that the mean stratiform vertical velocities were about $0.3\text{--}0.4 \text{ m s}^{-1}$ over a 8–14-km layer with peak values at $\sim 11\text{-km}$ altitude, and mean downdrafts

peaked at about 0.5 m s^{-1} from 2- to 3-km altitude. They obtained vertical motions from extended variable azimuth displays that provide more accurate mesoscale motions than those in the current study, which relies on proper removal of the hydrometeor fall speeds. The major differences in stratiform vertical motions observed for this case are 1) there are two separate regions of lifting rather than one widespread region as observed with previous cases, and 2) the mean ascent for this case is about two to three times larger than the largest stratiform vertical motions measured in previous cases (i.e., Rutledge et al. 1988).

The horizontal wind CFAD in the stratiform region shows that the rear inflow is confined to the lowest 2–3 km below the freezing level, and front-to-rear flow ($\sim -10 \text{ m s}^{-1}$) exists above this rear inflow. The squall line inflow to the east of the convective line has a few meter per second westward component, producing a relative flow of about -12 m s^{-1} and strong convergence just in advance of the squall line high-reflectivity leading edge. These flow differences are noted on the larger scale from the soundings (Figs. 5 and 6). The next section shows that this convergence provides strong forcing for the line.

c. Convective region

The leading convective region of the squall line is now examined using EDOP reflectivity and Doppler observations. EDOP also provides linear depolarization (LDR) measurements that provide useful microphysical information. LDR is defined by $10 \log(Z_n/Z_{hh})$, where Z_{ij} denotes reflectivity with i transmit polarization and j receive polarization. LDR is a function of the shape and canting of particles and the effective dielectric constant of scatterers; it increases significantly for particles such as liquid- or water-coated ice having a high dielectric constant (e.g., Doviak and Zrnic 1993; Herzegh and Jameson 1992). LDR for a similar wavelength airborne radar has been presented by Meneghini and Kumagai (1994). Figure 10 shows two-dimensional squall line–relative wind vectors (u, w) superimposed on the reflectivity, vertical hydrometeor motion, and LDR for the convective section of flight line 1 (426–456 km). Hydrometeor motion is presented instead of vertical velocity since small hail appeared to be present as will be discussed below. (Note that Fig. 8 focused on the stratiform region where fall speeds and vertical air motions were more reliably estimated.) As mentioned earlier, the forward Doppler measurements were degraded due to an instrument problem and hence wind vectors cover only the higher reflectivity regions.

The wind vectors in Fig. 10 depict inflow to the convective line from the east, a strongly tilted updraft region, and lower wind speeds in the trailing stratiform (where available). A distinct boundary is noted at about 448 km between the inflow air and undercutting from the 3-km-deep, low-level air behind the squall line, with

a pronounced rotor circulation in the gust front head. The vertical hydrometeor velocity panel shows a strongly tilted ($\sim 45^\circ$ angle) updraft region with a maximum core of $\sim 8 \text{ m s}^{-1}$ between 4- and 8-km altitude, and some stronger downdrafts aloft surrounding the convective region. The updraft comprises a number of discrete reflectivity and hydrometeor motion pulses, rather than being a continuous entity. This type of updraft appearance is similar to “stair stepped” updraft cores noted in and Smull and Houze (1987a). Whereas this may be due to the particular location of the cross section relative to the updraft maxima, updrafts in other cases with EDOP data have similar structures. Two-dimensional (e.g., Rotunno et al. 1988; Fovell and Ogura 1988) and three-dimensional (Trier et al. 1997) modeling studies have suggested that as squall lines mature, the convective cells sloped toward the upshear direction (i.e., toward the rear of the line). This is consistent with the current observations especially the presence of a strong rear inflow.

The observations suggest stratiform rain ahead of the line in addition to the previously discussed trailing region. Both a reflectivity and LDR bright band are present near the 2.5-km level, on the edges (i.e., distance $< 430 \text{ km}$ and $> 450 \text{ km}$) of the flight line segment presented in Fig. 10. The high LDR values (i.e., -10 to -15 dB) observed at the reflectivity bright band suggest partially melted, asymmetric aggregates, which are less oriented. Since the corresponding reflectivities are low, the hydrometeors are probably small in comparison with the intense portions of the trailing stratiform with reflectivities approaching 50 dBZ in the reflectivity bright band.¹ In the updraft region, the enhanced LDR zone is elevated to about 4 km and is wavy. Graupel or hail is likely between 438 and 443 km on the distance axis because high reflectivities $> 50 \text{ dBZ}$ are present between the surface and 4-km altitude and LDR values are high ($> -15 \text{ dB}$). In contrast, the high reflectivities ($45\text{--}50 \text{ dBZ}$) above 5 km in this region have somewhat lower LDR (-20 to -25 dB), consistent with drier ice particles with a low dielectric constant. Because LDR in the convective region below the freezing level is high, reflectivities are high, and the hydrometeor velocities are somewhat larger (-5 to -9 m s^{-1} between 3 and 5 km) than would be expected from partially melted snow, more dense ice hydrometeors such as conical graupel or hail are suggested. This is supported by the fact that a 4-mm-sized graupel with a terminal velocity $v_t = 3.62\sqrt{D} \text{ (mm)} \approx 7.2 \text{ m s}^{-1}$ is indicated using Matson and Huggins (1980) best-fit terminal velocity–diameter relation. A plausible explanation of these observations is that dry graupel or small hail falls out of the tilted updraft, becomes wetted above the freezing

¹ There could also be a lower concentration of particles but the size dependence (i.e., diameter to the sixth power) has a more dominant effect on the reflectivity.

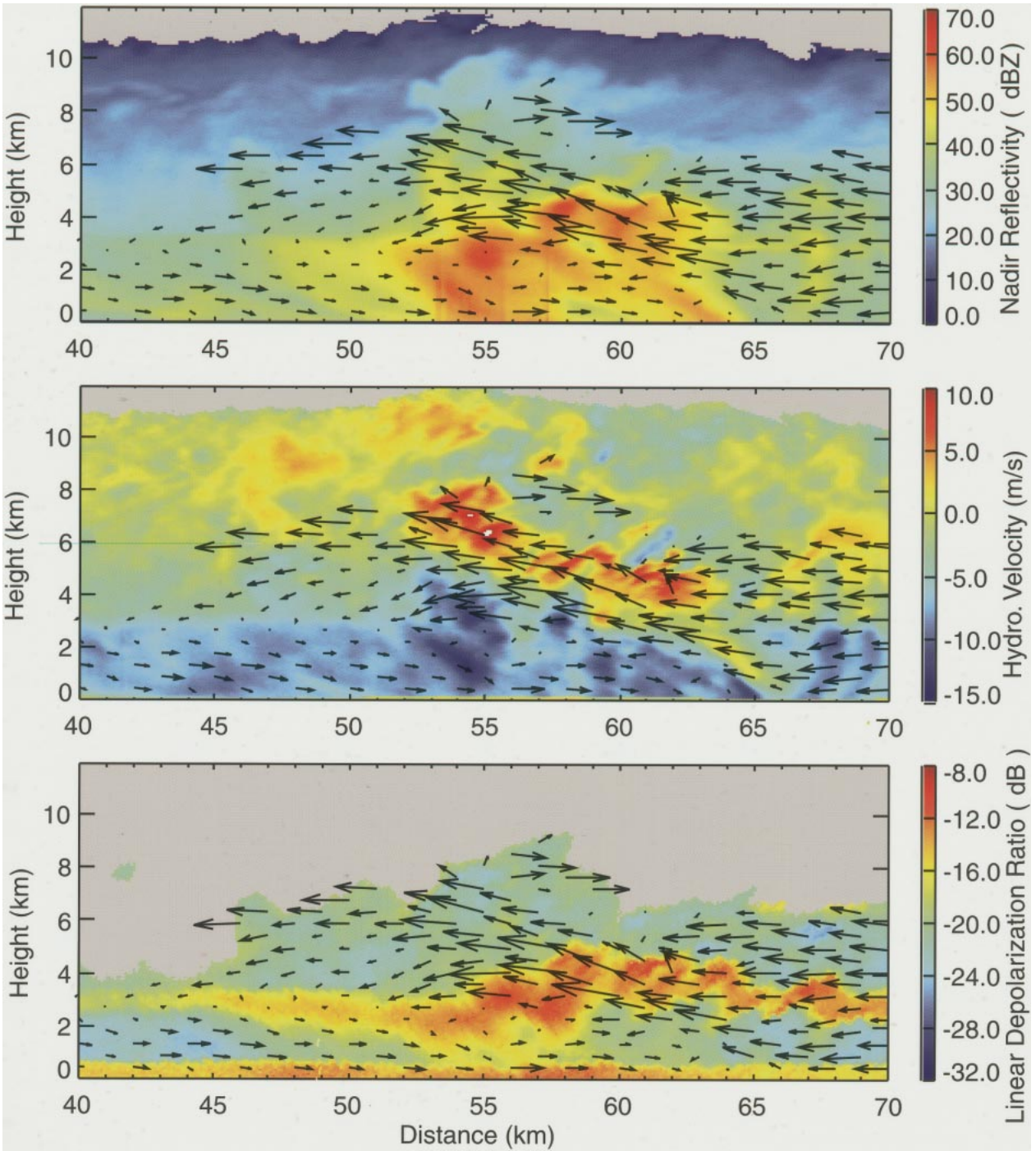


FIG. 10. Convective region of squall line extracted from line 1 in Fig. 8. Shown are nadir reflectivity, vertical hydrometeor motion, and (LDR) from flight line 1 (1730–1807). Position of this cross section is oriented with west on the left side and time increasing from left to right. Relative wind vectors are superimposed. See text for details.

level (producing a high LDR), and then reaches the surface before melting is completed. If indeed the ice particles were 4 mm in size, this small size would account for the lack of severe weather reports (i.e., hail) associated with the squall line.

d. Summary of squall line mesoscale structure

Figure 11 summarizes conceptually the coupling of the squall line with the larger-scale environment based on earlier analyses of conventional and EDOP obser-

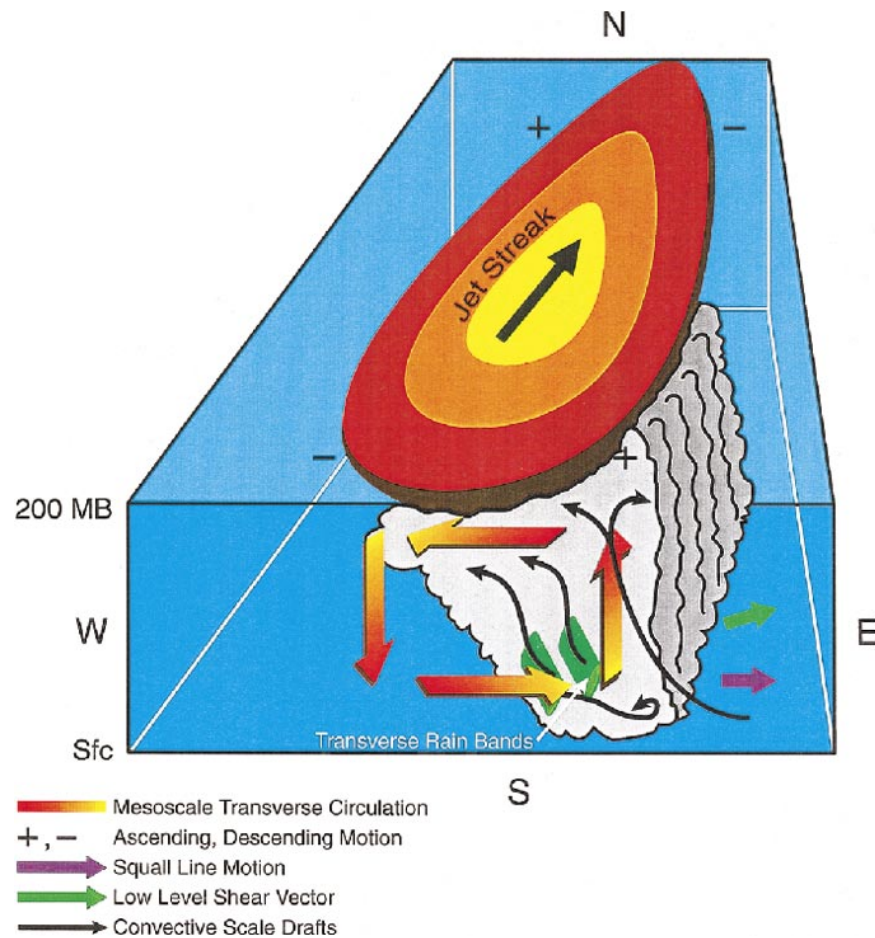


FIG. 11. Conceptual squall line structure deduced from radar and synoptic observations.

variations. The squall line updraft is tilted rearward toward the extensive stratiform region. A rear inflow undercuts the stratiform region and reaches the surface well behind the leading convective line near the rear edge of the stratiform rain. The relatively dry rear inflow has positive momentum and continues toward the east, undercutting the tilted updraft region. The EDOP observations suggest a density current head shown under the tilted updraft. Evaporation is likely to occur as the stratiform rain falls into the drier undercutting air, and a cold pool is established that helps maintain the squall line eastward propagation and density current.

The mesoscale vertical circulation in the jet streak entrance region provides favorable dynamics for sustaining the deep convective leading edge and the huge trailing stratiform region associated with the squall line. According to jet streak dynamics (e.g., Bluestein 1993), the right-rear quadrant of a jet streak favors upward vertical motions ($\omega < 0$). The dry air intrusion into the rear of the squall line and the front-to-rear ascending flow in the stratiform region may also be enhanced by the ageostrophic motion components produced by the

jet streak. Previous studies have linked low-level advection of high θ_e to a thermally indirect circulation in the exit region of a jet streak, priming the prestorm environment for deep convection. In contrast, this case suggests the thermally direct circulation in the entrance region of the jet is *part* of the air entering the squall line transverse circulation. Ageostrophic winds set up by the jet stream would interact synergistically with the squall line circulation, to help maintain the extensive 200-km-wide stratiform region. But with the given observations, one cannot determine the relative contributions of the large-scale and squall-line-scale forcing to the transverse circulation described above.

The rear inflow in the 13 January case is consistent with a direct vertical circulation set up in the right-rear entrance region of a jet streak. In previous studies, the rear inflow has been considered to be primarily a squall line-induced circulation. In the current case, the relative rear inflow (Fig. 6) produces strong leading-edge convergence as the westward component behind the line meets the low-level warm sector southeasterly flow ahead of the line.

5. Summary and conclusions

In this paper, we present an analysis of the Doppler observations from the EDOP radar overflying a wintertime squall line on 13 January 1995. The high-resolution vertical cross sections of reflectivity and Doppler velocities provided by EDOP give a unique view of the extensive stratiform region associated with the squall line. EDOP has the advantage of providing more detailed vertical structure than possible with conventional ground-based radars. Furthermore, mesoscale cross sections are obtained in a relatively short time interval compared with fixed (ground based) zenith-pointing radars and profilers. Mesoscale structure can change dramatically in just an hour's time as in the present case. This paper provides the first study to document the relation between high-resolution vertical velocity and reflectivity structure in convective and stratiform regions of a squall line, closely coupled with a larger-scale jet streak.

The squall line studied had several prominent features: 1) a strong, rearward-tilted, convective leading edge; 2) an extensive trailing stratiform region over 200 km in width; and 3) a 3-km-deep rear inflow descending to the surface well behind the leading edge and on the rear edge of the stratiform region. Whereas general features of the squall line resembled previous conceptual models of tropical and midlatitude squall lines, the stratiform region was large in comparison. The mean ascent in the stratiform region was several times larger than typical values reported in previous studies. These differences are suggested to be due to strong coupling between the squall line transverse circulation and jet stream dynamics. The squall line initiated east of an intensifying trough in the exit region of a jet maximum that set up a direct ageostrophic circulation. This larger-scale circulation was important in providing widespread lifting necessary to sustain the convective line and the extensive stratiform region. It also provided favorable conditions for rear inflow, which moved the system eastward and provided lifting along the convective leading edge. Finally, there was apparent gravity wave structure in the stratiform region indicated by two regions of enhanced vertical motion separated by about 100 km, which may be due to geostrophic adjustment processes. The squall line in the present study formed inside the exit region of a developing jet streak and gravity waves due to geostrophic adjustment have been observed frequently in this region (e.g., Uccellini and Koch 1987).

The squall line presented is complex due to its genesis in a broad region of prior convective lines and also the role of the larger-scale dynamics. Nevertheless, the rear-inflow characteristics agree in part with the results of Weisman (1992) whose modeling results showed that for environments with both weak to moderate vertical wind shear (10–15 m s⁻¹ in the lowest few kilometers) and CAPE (2000–3000 J kg⁻¹), the rear-inflow jet de-

scends and spreads along the surface nearly 200 km behind the leading edge. Although the rear inflow in the present case has this behavior and the environmental shear is consistent with these values, the CAPE values were extremely weak. It is clear that the synoptic-scale forcing in the present case is sufficiently strong that it would have to be included in the squall line modeling simulations. Furthermore, possible reasons why the rear inflow descends so far behind the leading edge are: 1) the characteristic width of the jet streak transverse circulation is approximately 200 km, and 2) the subsidence in the left jet streak entrance region is located at the back edge of the squall line anvil.

Coupling between the synoptic and squall line circulations as observed here has been reported infrequently in the literature. Most of the studies have focused on warm season squall lines where the squall line circulation itself is dominant. Similar types of systems have been studied recently by Chen et al. (1998) using TAMEX observations. To what extent these coupled systems as presented here are important requires further assessment.

The current dataset was fortuitously collected with minimal planning and supporting observations. Furthermore, some EDOP problems on this day prevented determination of the full two-dimensional squall line circulation with the EDOP observations. It is hoped that additional datasets can be obtained in the future that would provide more comprehensive measurements.

Acknowledgments. Thanks are due to several people in preparation of this manuscript. Dr. John Scala provided excellent forecasting for the aircraft flights and provided help in the initial analysis for this study. Dr. Steven Bidwell provided excellent engineering support for the EDOP instrument during the aircraft flights. Science discussions with Dr. Mohan Karampudi, Dr. Chang Chen, Dr. Scott Braun, Dr. Bart Geerts, and others are greatly acknowledged. In addition, several others were helpful with the analysis of datasets. Mr. George Lai provided help with the GEMPAK software especially in reading NGM datasets for analysis. Dr. Steve Goodman of Marshall Space Flight Center provided composite radar datasets, which were used to provide a general overview for the case. This work was supported under NASA's Mission to Planet Earth by Dr. Ramesh Kakar at NASA Headquarters.

APPENDIX

ER-2 Doppler Radar Description

a. Instrument description

EDOP is an X-band (9.6 GHz) Doppler radar system mounted in the NASA ER-2 aircraft's nose (Heymsfield et al. 1996b). Radial Doppler winds from the two beams are used to derive vertical and alongtrack air motions. In addition, the forward beam provides linear depolar-

ization (LDR) measurements, which are useful in discriminating microphysical characteristics of the precipitation. The system has two fixed beams: a nadir-oriented beam with a copolarized receiver and a 33° forward-directed beam with co- and cross-polarized receivers. The antennas have 2.97° beamwidths and a spot size of about 1.2 km at the surface (assuming a 20-km aircraft altitude). During HOPEX, EDOP was configured with 75-m gate spacing and a pulse repetition frequency of 4400 Hz providing a Nyquist velocity of about 34 m s^{-1} . Processed values were obtained every 0.5 s, which corresponds to approximately 100 m of aircraft translation (aircraft ground speed = 200 m s^{-1}). The data have been calibrated using the approach described in Caylor et al. (1994) but modified for several configuration changes during HOPEX. This provides an absolute calibration of about 1–2 dB in reflectivity. The mean Doppler velocity measurements have a standard deviation of about 0.1 m s^{-1} . During the 13 January flight, the forward Doppler channel exhibited poor sensitivity because of a defective cable; thus, the forward Doppler measurements are useful only for reflectivities greater than about 27 dBZ.

b. Calculation of u and w winds

Calculation of air motions from the measured Doppler velocities has been described in Heymsfield et al. (1996b). Two wind speeds can be calculated directly from combination of the forward and nadir Doppler velocities measured with EDOP: the vertical hydrometeor (v_h) component from which the vertical air motion (w) can be obtained with a hydrometeor fall speed (v_f) assumption, and the along-track horizontal component (u). A number of steps are involved in going from the measured EDOP Doppler velocities from the forward and nadir beams to these wind components. The forward beam Doppler velocities are first unfolded because of the large aircraft motion component. Then using Eq. (1) in Heymsfield et al. (1996b), the aircraft motions are removed from the Doppler velocities by using the information from inertial navigation system (INS) and the antenna tilt angles. Aircraft vertical motion required in this calculation is estimated to better than 0.5 m s^{-1} from integration of the vertical acceleration output of the INS and employing a third-order pressure feedback loop. The reflectivity measurements that can be attenuated by higher rain rates are corrected using a hybrid surface reference approach (Caylor et al. 1995), which performs well over water backgrounds as for the 13 January case.

To perform the dual-Doppler wind calculations for the horizontal winds, it is necessary to interpolate the measurements from the forward and nadir beams to a common grid. This grid is chosen with identical resolution to the nadir measurements (100 m horizontal, 75 m vertical). The u component can now be estimated from combination of the gridded Doppler velocities

through Eq. (5) in Heymsfield et al. (1996b). Note that the calculation of the u component requires only v_n and v_f and does not require v_t . But u is sensitive to aircraft attitude and navigation errors. A more significant problem with this dataset is that there was leakage in the intermediate frequency portion of the EDOP forward channel receiver, which produced an increased noise level in the forward Doppler velocity measurements. Thus forward Doppler measurements were ignored for reflectivities below roughly 27 dBZ.

Finally, filtering of the grids was performed both horizontally and vertically. Horizontal filtering of the vertical velocity and horizontal winds using a simple 100-point rectangular filter, highlight the mesoscale motions in the stratiform region. Because the forward beam is more smeared out in the vertical due to the 33.5° tilt of the radar pulse volumes (Heymsfield et al. 1996b), the vertical resolution of the nadir beam velocities was degraded with a 1.5-km wavelength low-pass filter in order to match the resolution of the two beams before their combination into horizontal winds.

Calculation of w requires estimation of the fall speeds at each grid point. The v_f estimate is the most critical assumption in obtaining w , since v_f depends on many factors such as particle phase, size distributions, etc. The following procedure is based on improvements to the approach used by Marks and Houze (1987) and Black et al. (1996). They used nadir and zenith Doppler velocities from the National Oceanic and Atmospheric Administration WP3 tail radar to provide vertical velocity estimates by removing hydrometeor motions v_t using $Z-v_t$ relations for the snow, rain, and intermediate transition regions. The latter paper mentions the difficulties in regions of strong convection where both liquid and frozen particles can exist simultaneously above the freezing level, and strong updrafts can carry liquid water, frozen rain, and graupel several kilometers above the melting level. These particles can have fall speeds ranging between those for rain and snow. Here an approach similar to the above studies is used although several improvements were required to the fall speed relations. These changes were necessary in part because the squall line case had extremely high reflectivities in both the stratiform and convective regions as compared with tropical storm studies. Also, the high-resolution measurements provided by EDOP define very narrow (few hundred meter thick) transition regions that cause derived vertical velocities to be somewhat sensitive to the assumed fall speed.

Fall speeds are estimated differently for stratiform and convective regions. Similar to Marks and Houze (1987) and Black et al. (1996), stratiform regions are separated vertically into three regions: rain, snow, and transition region corresponding to the melting layer. In these regions, the nadir beam Doppler velocities and reflectivities usually clearly define the Doppler velocity transition from snow with low fall speeds ($\sim 1 \text{ m s}^{-1}$) to rain with higher fall speeds ($\sim 6\text{--}9 \text{ m s}^{-1}$). The tran-

sition region top and bottom are estimated from first providing initial guess heights, and then examining the first derivative of Doppler velocity for large gradients. Usually, this defines the velocity transition to within one or two 75-m gates. Occasionally, weaker reflectivity regions with negligible bright bands do not have clearly defined velocity transitions; they are assumed missing. Later, these missing heights are interpolated or extrapolated from better-defined neighboring regions. The stratiform fall speeds v_R , v_S , and v_T in the rain, snow, and transition region are given in meters per second, respectively, by

$$v_R = \left(9.65 - 10.3 \left\{ 1 + 6 \left[\frac{Z}{N_0 10^6 \Gamma(7 + \mu)} \right]^{1/(7+\mu)} \right\}^{-(7+\mu)} \right) \times \left(\frac{\rho_0}{\rho} \right)^{0.45} \quad \text{for rain,} \quad (\text{A1})$$

$$v_S = 2.5 \left(\frac{6.0 - z}{6.0 - z_i} \right) (0.442 Z^{0.168}) \left(\frac{\rho_0}{\rho} \right)^{0.45} \quad \text{for snow, and} \quad (\text{A2})$$

$$v_T = \frac{(z_t - z)^2}{(z_t - z_b)^2} (v_R - v_S) + v_S \quad \text{for transition,} \quad (\text{A3})$$

where N_0 in units of $\text{m}^{-3} \text{cm}^{-1-\mu}$ and dimensionless μ are parameters in the gamma raindrop size distribution, Γ is the gamma function, Z is the radar reflectivity factor in $\text{mm}^6 \text{m}^{-3}$, and z_t , z_b , and z are, respectively, the top, bottom, and height in meters within the transition region. The density correction term, where ρ_0 , ρ are the air density at the surface and altitude z , respectively, assumes a coefficient of 0.45 according to Beard (1985). The v_R rain relation is a theoretical expression derived by Ulbrich and Chilson (1994), which is based on a gamma distribution. This relation, which is a modification of the equation derived by Atlas et al. (1973), is significantly better than the power law $Z-v_t$ relations used for tropical storms. The power law relations increase monotonically with higher reflectivities instead of converging asymptotically to approximately 9.65 m s^{-1} as found observationally by Gunn and Kinzer (1949). The range of the parameters in the gamma distribution was estimated by nonlinear least squares fitting of the v_R relation above using Doppler velocity–reflectivity pairs from the stratiform rain region. This resulted in typical values of N_0 and μ of approximately 100 and -1.5 , respectively, and should provide v_t to better than 1 m s^{-1} in rain regions. The gamma distribution fall speed curves are plotted for $\mu = 0, 2$, and 4 in Fig. A1, where the solid “RAIN” curve was used for removing rain fall speeds in this paper. Also, the power

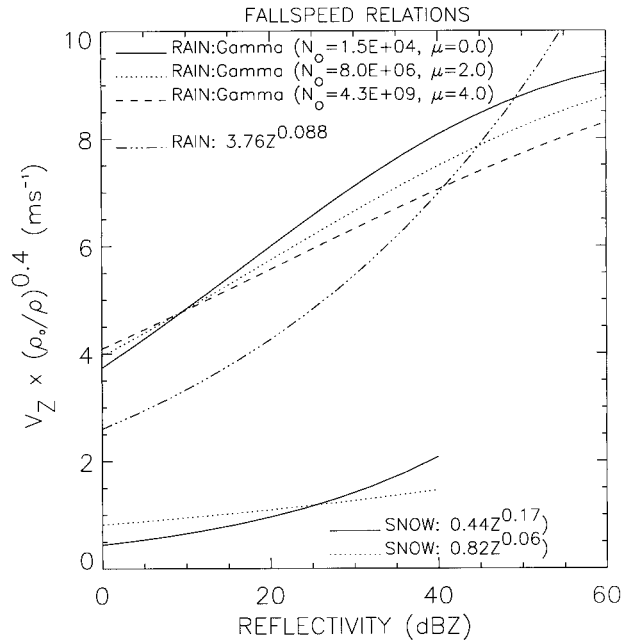


FIG. A1. Fall speed relations used for calculating vertical air motions from Doppler velocities; N_0 has units of $\text{m}^{-3} \text{cm}^{-1-\mu}$ and μ is dimensionless. Solid curves used for removing hydrometeor motions from Doppler velocities. See text for details.

law relation used by Black et al. (1996) is shown along with the three Gamma curves for reference.

Several snow relations in the literature (e.g., Atlas et al. 1973) were tested on the EDOP dataset. None of these fit the data well so it was decided to obtain a relation by fitting the actual density-corrected Doppler velocity and reflectivity pairs with a power law relation. This fitted relation given in (A1) was used throughout the snow region, and it is shown by the solid “SNOW” curve in Fig. A1. For reference, the snow fall speed relation from Atlas et al. (1973) is shown by dashed “SNOW” curve. The transition region fall speeds are given by the parabolic relation in (A2), which fits the velocity observations better than a linear relation as used by Marks and Houze (1987).

The squall line convective region is defined by vertical profiles with reflectivities greater than 45 dBZ in the 0–6-km layer. For regions with reflectivities higher than 45 dBZ above the rain region, the v_R relation is used. Difficulty occurs in mixed-phase regions and when large ice particles (hail) are present and errors are somewhat larger. In particular, just to the rear of the convective region in Fig. 9, large LDR below the melting level indicated the presence of dense hydrometeors such as graupel. Lump graupel has fall speeds of a few meters per second (e.g., Mitchell 1996), which is between the snow and rain fall speeds in (A1) and (A2). As a result, it was decided to multiply fall speeds in the snow region according to (A3), which assumes graupel near the melting level, snow at 6-km altitude, and a linear transition between z_t and 6-km altitude. These relations are con-

sistent with the vertical hydrometeor motions but imply that the fall speeds are subject to errors possibly a few meters per second in the convective region.

REFERENCES

- Atlas, D., R. C. Srivastava, and R. S. Sekhon, 1973: Doppler radar characteristics of precipitation at vertical incidence. *Rev. Geophys. Space Phys.*, **11**, 1–35.
- Beard, K. V., 1985: Simple altitude adjustments to raindrop velocities for Doppler radar analysis. *J. Atmos. Oceanic Technol.*, **2**, 468–471.
- Biggerstaff, M. I., and R. A. Houze Jr., 1991: Kinematics and precipitation structure of the 10–11 June 1985 squall line. *Mon. Wea. Rev.*, **119**, 3034–3065.
- , and —, 1993: Kinematics and microphysics of the transition zone of the 10–11 June 1985 squall line. *J. Atmos. Sci.*, **50**, 3091–3110.
- Black, M. L., R. W. Burpee, and Frank D. Marks Jr., 1996: Vertical motion characteristics of tropical cyclones determined with airborne Doppler radial velocities. *J. Atmos. Sci.*, **53**, 1887–1909.
- Bluestein, H. B., 1993: *Observations and Theory. Synoptic-Dynamic Meteorology in Midlatitudes*. Vol. II. Oxford University Press, 594 pp.
- , and M. H. Jain, 1985: Formation of mesoscale lines of precipitation: Severe squall lines in Oklahoma during spring. *J. Atmos. Sci.*, **42**, 1711–1732.
- Carbone, R. E., 1982: A severe frontal rainband. Part I: Stormwide hydrodynamic structure. *J. Atmos. Sci.*, **39**, 258–279.
- Caylor, I. J., G. M. Heymsfield, S. Bidwell, and S. Ameen, 1994: NASA ER-2 Doppler radar reflectivity calibration for the CAMEX project. NASA Tech. Memo. 104611, 15 pp. [Available from NASA Center for Aerospace Information, 800 Elkridge Landing Rd., Linthicum Heights, MD 21090-2934.]
- , —, —, and —, 1995: Estimating the rain rate profile in the presence of attenuation using EDOP airborne radar observations. Preprints, *27th Radar Meteorology Conf.*, Vail, CO, Amer. Meteor. Soc., 783–785.
- Chen, C., W.-K. Tao, P.-L. Lin, G.S. Lai, S.-F. Tseng, and T.-C. C. Wang, 1998: The intensification of the low-level jet during the development of mesoscale convective systems on a Mei-Yu front. *Mon. Wea. Rev.*, **126**, 349–371.
- Crum, T. D., R. L. Alberty, and D. W. Burgess, 1993: Recording, archiving, and using WSR-88D data. *Bull. Amer. Meteor. Soc.*, **74**, 645–653.
- Doviak, R. J., and D. S. Zrnic, 1993: *Doppler Radar and Weather Observations*. Academic Press, 267–268.
- Fovell, R. G., and Y. Ogura, 1988: Numerical simulation of a mid-latitude squall line in two dimensions. *J. Atmos. Sci.*, **45**, 3846–3879.
- Gunn, R., and G. D. Kinzer, 1949: The terminal velocity of fall for water droplets in stagnant air. *J. Meteor.*, **6**, 243–248.
- Halverson, J. B., B. J. Ferrier, T. M. Rickenbach, J. Simpson, and W.-K. Tao, 1999: An ensemble of convective systems on 11 February 1993 during TOGA COARE: Morphology, rainfall characteristics, and anvil cloud interactions. *Mon. Wea. Rev.*, **127**, 1208–1228.
- Herzogh, P. H., and A. R. Jameson, 1992: Observing precipitation through dual-polarization radar measurements. *Bull. Amer. Meteor. Soc.*, **73**, 1365–1374.
- Heymsfield, G. M., I. J. Caylor, J. M. Shepherd, W. S. Olson, S. W. Bidwell, W. C. Boncyk, and S. Ameen, 1996a: Structure of Florida thunderstorms using high-altitude aircraft radiometer and radar observations. *J. Appl. Meteor.*, **35**, 1736–1762.
- , and Coauthors, 1996b: The EDOP radar system on the high altitude NASA ER-2 aircraft. *J. Atmos. Oceanic Technol.*, **13**, 795–809.
- Hildebrand, P., and Coauthors, 1996: The ELDORA/ASTRAIA airborne Doppler radar: High-resolution observations from TOGA COARE. *Bull. Amer. Meteor. Soc.*, **77**, 213–232.
- Houze, R. A., Jr., 1977: Structure and dynamics of a tropical squall-line system. *Mon. Wea. Rev.*, **105**, 1540–1567.
- , and P. V. Hobbs, 1982: Organization and structure of precipitating cloud systems. *Advances in Geophysics*, Vol. 24, Academic Press, 225–315.
- , B. F. Smull, and P. Dodge, 1990: Mesoscale organization of springtime rainstorms in Oklahoma. *Mon. Wea. Rev.*, **118**, 613–654.
- Koch, S. E., M. desJardins, and P. J. Kocin, 1983: An interactive Barnes objective map analysis scheme for use with satellite and conventional data. *J. Climate Appl. Meteor.*, **22**, 1487–1503.
- LeMone, M. A., E. Zipser, and S. B. Trier, 1998: The role of environmental shear and CAPE in determining the structure and evolution of mesoscale convective systems during TOGA COARE. *J. Atmos. Sci.*, **55**, 3493–3518.
- Marks, F. D., Jr., and R. A. Houze Jr., 1987: Inner core structure of Hurricane Alicia from airborne Doppler radar observations. *J. Atmos. Sci.*, **44**, 1296–1317.
- Matson, R. J., and A. W. Huggins, 1980: The direct measurement of the sizes, shapes, and kinematics of falling hailstones. *J. Atmos. Sci.*, **37**, 1107–1125.
- Meneghini, R., and H. Kumagai, 1994: Characteristics of the vertical profiles of dual-frequency, dual-polarization radar data in stratiform rain. *J. Atmos. Oceanic Technol.*, **11**, 701–711.
- Mitchell, D. L., 1996: Use of mass- and area-dimensional power laws for determining precipitation particle terminal velocities. *J. Atmos. Sci.*, **53**, 1710–1723.
- Pruppacher, H. R., and J. D. Klett, 1997: *Microphysics of Clouds and Precipitation*. Kluwer Academic, 954 pp.
- Rotunno, R., J. B. Klemp, and M. L. Weisman, 1988: A theory for strong, long-lived squall lines. *J. Atmos. Sci.*, **45**, 463–485.
- Rutledge, S. A., R. A. Houze Jr., M. Biggerstaff, and T. Matejka, 1988: The Oklahoma–Kansas mesoscale convective system of 10–11 June 1985: Precipitation structure and single-Doppler radar analysis. *Mon. Wea. Rev.*, **116**, 1409–1430.
- Smull, B. F., and R. A. Houze, 1987a: Dual-Doppler radar analysis of a mid-latitude squall line with a trailing region of stratiform rain: radar and satellite observations. *J. Atmos. Sci.*, **44**, 2128–2148.
- , and —, 1987b: Rear inflow in squall lines with trailing stratiform precipitation. *Mon. Wea. Rev.*, **115**, 2869–2889.
- Trier, S. B., W. C. Skamarock, and M. A. LeMone, 1997: Structure and evolution of the 22 February 1993 TOGA COARE squall line: Organization mechanisms inferred from numerical simulation. *J. Atmos. Sci.*, **54**, 386–407.
- Uccellini, L. W., and D. R. Johnson, 1979: The coupling of upper and lower tropospheric jet streaks and implications for the development of severe convective storms. *Mon. Wea. Rev.*, **107**, 682–703.
- , and S. E. Koch, 1987: The synoptic setting and possible energy sources for mesoscale wave disturbances. *Mon. Wea. Rev.*, **115**, 721–729.
- Ulbrich, C. W., and P. B. Chilson, 1994: Effects of variations in precipitation size distribution and fallspeed law parameters on relations between mean Doppler fallspeed and reflectivity factor. *J. Atmos. Oceanic Technol.*, **11**, 1656–1663.
- Weisman, M. L., 1992: The role of convectively generated rear inflow jets in the evolution of long-lived mesoconvective systems. *J. Atmos. Sci.*, **49**, 1826–1847.
- , J. B. Klemp, and R. Rotunno, 1988: Structure and evolution of numerically simulated squall lines. *J. Atmos. Sci.*, **45**, 1990–2013.
- Yuter, S. E., and R. A. Houze Jr., 1995: Three-dimensional kinematic and microphysical evolution of Florida cumulonimbus. Part II: Frequency distributions of vertical velocity, reflectivity, and differential reflectivity. *Mon. Wea. Rev.*, **123**, 1941–1958.